



Please cite the Published Version

Bai, Wei , Feng, Xingya, Jiang, Sheng-Chao, Cong, Peiwen and Qian, Ling  (2024) Suppression of the second harmonic induced wave near-trapping around a cylinder array. *Applied Ocean Research*, 153. 104209 ISSN 0141-1187

DOI: <https://doi.org/10.1016/j.apor.2024.104209>

Publisher: Elsevier

Version: Published Version

Downloaded from: <https://e-space.mmu.ac.uk/635403/>

Usage rights:  [Creative Commons: Attribution 4.0](https://creativecommons.org/licenses/by/4.0/)

Additional Information: This is an open access article which first appeared in *Applied Ocean Research*, published by Elsevier

Data Access Statement: Data will be made available on request.

Enquiries:

If you have questions about this document, contact openresearch@mmu.ac.uk. Please include the URL of the record in e-space. If you believe that your, or a third party's rights have been compromised through this document please see our Take Down policy (available from <https://www.mmu.ac.uk/library/using-the-library/policies-and-guidelines>)



Invited paper

Suppression of the second harmonic induced wave near-trapping around a cylinder array

Wei Bai^{a,*}, Xingya Feng^b, Sheng-Chao Jiang^c, Peiwen Cong^d, Ling Qian^a

^a Department of Computing and Mathematics, Manchester Metropolitan University, Chester Street, Manchester M1 5GD, UK

^b Department of Ocean Science and Engineering, Southern University of Science and Technology, Shenzhen, 518055, China

^c School of Naval Architecture, State Key Laboratory of Structural Analysis for Industrial Equipment, Dalian University of Technology, Dalian 116024, China

^d State Key Laboratory of Coastal and Offshore Engineering, Dalian University of Technology, Dalian 116024, China

ARTICLE INFO

Keywords:

Near-trapping
Second-order time-domain method
Mass-spring system
Suppression
Second harmonic

ABSTRACT

Near-trapping is an essential resonant phenomenon associated with multiple-column structures in water waves, which exhibits high wave profiles in the area enclosed by multiple columns. For engineering safety, a straightforward scenario is proposed in this study to suppress the near-trapping phenomenon by allowing the multiple columns to move longitudinally with respect to the symmetric axes. To evaluate the effectiveness of the scenario, a stable and efficient second-order numerical model in the time domain is developed and adopted, which is also robust for the simulation of multiple structures with complex geometry and undergoing individual motions. Since both the first-order and second-order boundary value problems are solved, the second-order nonlinear properties are highlighted and the second harmonic induced near-trapping is the main focus of this study. For the cases in this study, the numerical results obtained by the validated numerical model confirm that this scenario can reduce the maximum second harmonic of the wave elevation by 63% and the maximum second-order wave elevation by 59% at the second near-trapping frequency. The first-order wave elevation is also reduced, and it is even smaller than the incident wave in a large portion of the enclosed region. As a mass-spring system is considered in the simulation of body responses, by testing different body masses and stiffnesses, it is revealed that the wave profile is insensitive to those parameters and the reduction in the wave profile occurs for all those parameters tested. It is interesting to find out that the near-trapping frequency can shift in the suppression scenario, and a remarkable reduction (32%) in the second-order wave elevation is still observed at the shifted near-trapping frequency.

1. Introduction

In recent years, in addition to traditional industrial activities in the ocean, such as oil and gas exploration and production, and ship transportation, the offshore industry has expanded to many new emerging domains including renewable energy utilisation, ocean aquaculture and deep sea mining. Those new domains offer plenty of opportunities but also bring lots of challenges, which has been attracting more effort devoted to addressing various impactful problems in engineering practice. Offshore structures are the essential platform to ensure that all offshore activities are conducted in a safe and efficient environment. Among different types of offshore structures, column-based platforms including the widely used semi-submersibles and tension leg platforms have a large share in the current market, where the multiple columns can enclose an area on the water surface. Some issues arise at certain wave frequencies due to the high wave elevations in this enclosed area and the large wave forces exerted on the columns, which affect directly

the design of the air gap of the deck and the strength of the column. As the wave energy seems to be trapped in the enclosed area caused by the wave diffraction and re-diffraction, this phenomenon is known as near-trapping.

The pioneering work on near-trapping waves induced by arrays of vertical circular cylinders using the analytical analysis was conducted in [Evans and Porter \(1997\)](#) by the linear potential flow theory. The study demonstrated the large peaks in the forces on an array of circular cylinders when the near-trapped mode corresponds to a near standing wave motion. [Maniar and Newman \(1997\)](#) analytically studied similar near-trapping modes between adjacent cylinders in a long finite array at critical wave numbers and found these modes were associated with the existence of homogeneous solutions for the diffraction by a cylinder array. [Malenica et al. \(1999\)](#) developed a semi-analytical approach to study the wave diffraction around an array of bottom-mounted circular cylinders, where the second-order potential was solved directly using

* Corresponding author.

E-mail address: w.bai@mmu.ac.uk (W. Bai).

eigenfunction expansions. The near-trapping phenomenon induced by the second harmonic was reported in second-order monochromatic waves. More recently, the regular wave interaction with arrays of elliptical cylinders was investigated in [Chatjigeorgiou and Katsardi \(2018\)](#), where the analytical solution to the problem was derived based on the linear potential flow theory. To handle this special geometry, the elliptic coordinate system was transferred for the elliptical harmonics. The results verified that any array of elliptical cylinders is also potentially a wave-trapping configuration. This analytical approach was extended to the study of an array of truncated cylinders in a perpendicular arrangement in front of a vertical breakwater, as shown in [Konispoliatis et al. \(2020\)](#). The image method was used for the bodies in front of the breakwater that was simulated by an elliptical cylinder with a zero semi-minor axis. Again, the near-trapped mode was identified in the study. In a more recent study of [Konispoliatis \(2023\)](#), wave near-trapping around an array of porous circular cylinders was captured and the effects of porous parameters and geometrical configurations were explored. [Li et al. \(2023\)](#) developed a model for wave scattering by porous cylinders with the presence of a vertical wall, where the wave amplitude becomes smaller due to the adoption of porous cylinders. Analytical solutions were also obtained recently for an array of floating cylinders with potential applications to wave energy converters in [Kang et al. \(2024\)](#). Apart from the frequency-domain solutions, a time-domain solution for studying the near-trapping was derived in [Meylan and Eatock Taylor \(2009\)](#) who used a generalised eigenfunction expansion method to approximate the near-trapped mode shapes with incident waves as wave groups.

A few experiments have been carried out to demonstrate the existence and characteristics of the near-trapping around cylinder array in the physical wave tank. For example, [Ohl et al. \(2001a\)](#) and [Ohl et al. \(2001b\)](#) experimentally investigated the near-trapping of an array of four cylinders in regular and irregular waves, respectively. In addition, both first-order and second-order near-trapping phenomena were illustrated through measured wave runup and wave forces in [Contento et al. \(2005\)](#). The near-trapping motions of a column-supported platform were also observed in the experiment in [Wolgamot et al. \(2016\)](#). Nonetheless, numerical simulation is still the main method to tackle the near-trapping problem. The second-order numerical model in the frequency domain was used in [Walker et al. \(2008\)](#) to investigate the near-trapping around an array of four cylinders. Both the first-order and second-order near-trappings were identified in monochromatic waves, and the study was further extended to consider NewWave as the incident wave. With the same numerical model, [Grice et al. \(2013\)](#) presented the influence of column shape and geometrical arrangement of columns on the near-trapping phenomenon, and an approximation of near-trapping mode shapes was developed in [Grice et al. \(2015\)](#). [Chen et al. \(2012\)](#) developed another efficient solver for the first-order model using the null-field boundary integral equation, and adopted the developed numerical model to carry out the parametric study on the near-trapping. The more recent work includes one reported in [Ren et al. \(2021\)](#), where commercial software was used for the same second-order problem, and the main focus was on assessing the influence of different corner ratios for four squared columns on the near-trapping. In addition, [Cong et al. \(2023\)](#) presented another numerical solution to the bi-chromatic wave interaction with vertical columns in a square arrangement. Both the circular cylinders and squared cylinders with rounded corners were considered using the second-order numerical model in the frequency domain, where an approximation approach was further developed to predict the second-order near-trapping responses.

In terms of the time-domain simulation, [Wang and Wu \(2007\)](#) used the finite element method to solve numerically the second-order potential flow model in the time domain for the study of the near-trapped mode around multiple circular cylinders. This numerical model has recently been extended in [Yang and Wang \(2020\)](#) to include the current in the problem by defining a zero-order problem for the current. With the developed numerical model, the near-trapping phenomenon

was analysed for multiple cylinders in a combined water wave and uniform current, and the influence of current speed was highlighted. [Wang et al. \(2024\)](#) considered again the effect of the presence of a uniform current on the near-trapping in an array of four cylinders and found the nonlinearity was enhanced by the current. To simulate the results beyond the second order, a fully nonlinear potential flow model was applied to study the near-trapping phenomenon around an array of vertical circular cylinders in [Bai et al. \(2014\)](#). In this study, by using the FFT analysis the first, second and third harmonics were extracted, from which a different trapped mode excited by the third harmonic was identified. Furthermore, the viscous flow model has also been used in the study of the near-trapping phenomenon by solving the Navier–Stokes equations with an open-source software package, as shown in [Lin et al. \(2020\)](#). An integrated wave-structure-seabed interaction model was developed to study the near-trapping effects on the dynamic response of the seabed and the liquefaction around the cylinder foundation. It should be mentioned that [Ning et al. \(2022\)](#) developed a Boussinesq model based on the cut cell technique to reveal some physical mechanisms of the near-trapping in a four-cylinder array.

It is evident that all the previous work discussed above focused on the identification of the near-trapping phenomenon and how the near-trapping behaves at various configurations for stationary multiple columns in different wave conditions. Given that near-trapping exhibits high wave elevations and large wave forces, it naturally leads to the next question of how to suppress the near-trapping. The suppression of near-trapping has been tackled by [Ning et al. \(2022\)](#) in their Boussinesq modelling, where the positions of the cylinders were changed in order to destroy the geometrical symmetry of the system. This scenario was demonstrated to be effective, however, it may not be preferable in realistic offshore practice, which motivates the present work. In this study, the symmetric feature of the system is retained, but the cylinders are allowed to move in certain directions as a mass–spring system to reduce the significant wave amplitude in the near-trapping. This is a new and the first meaningful attempt in the suppression of near-trapping. This idea is straightforward, as it is known that the dynamic response of a structure in waves can absorb the wave energy, so as to reduce the wave profile around the structure. In order to implement those scenarios to suppress the near-trapping, a second-order numerical model in the time domain is developed and adopted in this study, which is capable of simulating multiple structures undergoing different motions individually in water waves.

The second-order time-domain method is a classical method, first proposed in [Isaacson and Cheung \(1992\)](#) and [Isaacson and Ng \(1995\)](#). Other applications of this method include [Wang and Wu \(2007\)](#), [Yang and Wang \(2020\)](#) using the finite element method, [Bai and Teng \(2013\)](#) using the B-spline based boundary element method, and [Shao and Faltinsen \(2010\)](#) and [Shao et al. \(2022\)](#) using the high-order boundary element method. This method is only valid for weakly nonlinear problems, i.e. the incident wave steepness ϵ is mild, and the body response is also moderate compared to the typical size of the structure if the structure is free to move. Nevertheless, this method has its unique advantages compared to other popular methods on the basis of the potential flow theory. First of all, it is in the time domain, therefore, it can provide more information on evolution, especially for non-periodic problems. In addition, the second-order time-domain method can, on the one hand, provide second-order properties, which can consider more nonlinearity compared to the first-order method. On the other hand, this method is much more efficient computationally compared to the fully nonlinear method, with the compromise of ignoring third- and higher-order nonlinear components. However, due to the complexity of the problem, the present work demands a more robust numerical model, which is able to simulate multiple bodies with individual motion on each body. None of the previous second-order time-domain models has reported/demonstrated its capability in simulating the dynamic responses of multiple bodies. As multiple bodies can cause difficulties in creating the parametric space for the B-spline function in the B-spline

based boundary element method (Bai and Teng, 2013), in conjunction with the ordinary higher-order boundary element method (Bai and Eatock Taylor, 2006), a new numerical model is developed in the present study for the second-order time-domain method described in Bai and Teng (2013). This new numerical model has the required robustness for moving multiple bodies, and it is also stable and efficient. After the convergence test and validation, the numerical model is implemented in the evaluation of the effectiveness of two scenarios in suppressing the near-trapping phenomenon, and some interesting findings are reported for the first time.

2. Mathematical formulation and numerical method

It is well known that the problem of water wave interaction with marine structures can be modelled by the potential flow theory when the structure is relatively large compared to the wavelength. Under the assumptions of the incompressible and inviscid fluid with irrotational motions, a velocity potential ϕ exists, which satisfies the following Laplace equation within the computational domain:

$$\nabla^2 \phi = 0, \quad (1)$$

where the gradient of the velocity potential ϕ represents the velocity field. To construct the boundary value problem for solving the velocity potential, various boundary conditions need to be specified on all the boundary surfaces of the computational domain, including the free surface S_F , the seabed (which is horizontal in this study) S_D , the body surface S_B and the far field boundary to avoid the unwanted wave reflection.

2.1. Second-order time-domain method

In this boundary value problem, the governing equation is linear; while the free surface boundary conditions are nonlinear, which are also satisfied on the unknown instantaneous free surface. This is the main difficulty one has to face when solving this problem. Furthermore, the introduction of moving bodies in the domain requires the body condition to be applied on the instantaneous wetted body surface. There are many different approaches to tackling the difficulties of the problem, and here in this study, the second-order method in the time domain is used.

To formulate the first-order and second-order boundary value problems, the same procedure as in Bai and Teng (2013) is adopted. The Taylor series expansions to the free surface and body surface boundary conditions and the Stokes perturbation procedure can separate the problem into different orders by retaining terms at the order of wave steepness ϵ and ϵ^2 , respectively. Moreover, in the Stokes perturbation series, the velocity potential ϕ and the wave elevation η are further divided as

$$\phi = \phi^w + \phi^s; \quad \eta = \eta^w + \eta^s, \quad (2)$$

where the superscripts w and s denote the incident wave and scattered wave components respectively. The incident wave components are known from the Stokes wave theory; while the scattered wave components are caused by the presence of the body in the computational domain and to be solved as the unknowns of the problem.

With the use of the Taylor series expansion, the computational domain is now reduced to a time-invariant domain with the boundary conditions satisfied on the mean position of the moving boundary surfaces, which can much simplify the computation in terms of the computational effort and numerical robustness. In the time-invariant domain, for the first-order ($j = 1$) and second-order ($j = 2$) boundary value problems, the scattered velocity potential satisfies the Laplace equation,

$$\nabla^2 \phi_j^s = 0. \quad (3)$$

The corresponding boundary conditions for the scattered velocity potential are defined on the still water surface S_0 , the mean body surface S_b and the horizontal seabed S_D . Note that in this study the structure can only experience the translational motions ξ , where $\xi = (\xi_x, \xi_y, \xi_z)$ denotes the displacements of surge, sway and heave, respectively. In the following discussion, for the sake of simplicity, the rotational motions are ignored, however, the full formulation for the six-degrees-of-freedom motions can be found in Bai and Teng (2013) and the developed numerical model has the capability of simulating both the translational and rotational motions. The boundary conditions for the first-order and second-order boundary value problems read:

$$\frac{\partial \phi_j^s}{\partial z} - \frac{\partial \eta_j^s}{\partial t} = \begin{cases} 0, & j = 1 \\ -\left(\frac{\partial \phi_1^w}{\partial z} - \frac{\partial \eta_1^w}{\partial t}\right) + \frac{\partial \phi_1}{\partial x} \frac{\partial \eta_1}{\partial x} + \frac{\partial \phi_1}{\partial y} \frac{\partial \eta_1}{\partial y} - \eta_1 \frac{\partial^2 \phi_1}{\partial z^2}, & j = 2 \end{cases} \quad \text{on } S_0, \quad (4)$$

$$\frac{\partial \phi_j^s}{\partial t} + g\eta_j^s = \begin{cases} 0, & j = 1 \\ -\left(\frac{\partial \phi_2^w}{\partial t} + g\eta_2^w\right) - \frac{1}{2} |\nabla \phi_1|^2 - \eta_1 \frac{\partial^2 \phi_1}{\partial z \partial t}, & j = 2 \end{cases} \quad \text{on } S_0, \quad (5)$$

$$\frac{\partial \phi_j^s}{\partial n} = \begin{cases} -\frac{\partial \phi_1^w}{\partial n} + \xi_1 \cdot \mathbf{n}, & j = 1 \\ -\frac{\partial \phi_2^w}{\partial n} + \xi_2 \cdot \mathbf{n} - [\xi_1 \cdot \nabla (\nabla \phi_1)] \cdot \mathbf{n}, & j = 2 \end{cases} \quad \text{on } S_b, \quad (6)$$

$$\frac{\partial \phi_j^s}{\partial z} = 0 \quad \text{on } S_D. \quad (7)$$

Note that the space-fixed coordinate system $Oxyz$ has its origin O on the still water level, with the z axis pointing vertically upwards. In the equations, \mathbf{n} is the unit normal vector pointing out of the fluid domain, g is the gravitational acceleration, and all the subscripts ($j = 1$ or 2) denote the order of the properties. In addition, the body responses ξ_1 and ξ_2 need to be determined by the equation of motion based on Newton's second law, which will be discussed later. For some cases in this study when the structure is fixed, both two body response components are just specified as zero.

2.2. Numerical method

The first-order and second-order boundary value problems have to be solved numerically for the problem being investigated in the present study. In the higher-order boundary element method, a Rankine source is adopted as the Green function G , by which a boundary integral equation for the velocity potential ϕ over the entire boundary surface S of the computational domain is obtained using the Green's second identity:

$$C(\mathbf{x}_0)\phi(\mathbf{x}_0) = \iint_S \left[G(\mathbf{x}, \mathbf{x}_0) \frac{\partial \phi(\mathbf{x})}{\partial n} - \phi(\mathbf{x}) \frac{\partial G(\mathbf{x}, \mathbf{x}_0)}{\partial n} \right] ds, \quad (8)$$

where \mathbf{x} and \mathbf{x}_0 are the source point and field point, respectively, and C is the solid angle. The discretisation of the boundary integral equation to assemble the matrix for the unknowns is detailed in Bai and Eatock Taylor (2006).

However, during the discretisation, the second derivative of the first-order velocity potential in the body boundary condition Eq. (6) needs to be evaluated, which could limit the accuracy of the numerical simulation, as it is always a challenging task to calculate higher derivatives accurately using the boundary element method with the computational elements distributed on the boundary surfaces. To overcome the difficulty, a transformation has been proposed in Bai and Teng (2013), which is also adopted in this study. In the boundary integral equation, the term involving the second derivative is isolated and expressed as

$$\iint_{S_b} G [\xi_1 \cdot \nabla (\nabla \phi_1)] \cdot \mathbf{n} ds. \quad (9)$$

By using the Stokes formula, the above integral can be transformed to the following expression,

$$\iint_{S_b} [\xi_1 (\nabla G \cdot \nabla \phi_1) - \nabla \phi_1 (\nabla G \cdot \xi_1)] \cdot \mathbf{n} ds + \oint_{wl} G (\nabla \phi_1 \times \xi_1) \cdot d\mathbf{l}, \quad (10)$$

where wl denotes the water line where the structure intersects with the still water level. It can be seen that the second derivative can now be calculated using the first derivatives and a line integral on the still water surface, which can improve the accuracy of the simulation.

2.3. Numerical implementation

Since the incident wave is specified according to the Stokes wave theory within the entire computational domain, the numerical calculation is conducted in a circular tank, where the wave-making facility is unnecessary. On the side wall of the circular numerical wave tank, structured quadrilateral meshes are distributed. For structures with simple geometry, such as the vertical circular cylinder considered in this study, structured quadrilateral meshes are adopted as well to discretise the structure surface. For complicated structures, such as the supporting structure of offshore wind turbines, unstructured triangular meshes can be generated by mesh generation software and then imported into the present numerical model. Unstructured triangular meshes are also generated on the arbitrarily complicated free water surface using the Delaunay triangulation method. Therefore, the present numerical model is able to handle any complicated geometry with both the structured quadrilateral meshes and the unstructured triangular meshes.

As used in Bai and Eatock Taylor (2006), the artificial damping layer is allocated at the far end part of the circular wave tank on the water surface, to damp out the wave energy of the induced scattered wave before it reaches the far end wall and causes the reflection. In addition, the fourth-order Runge–Kutta scheme is used to update the kinematic free surface boundary condition for η and the dynamic free surface boundary condition for ϕ . As the incident wave is imposed in the flow field, the abrupt change in the boundary conditions needs to be avoided. In this study, a cosine ramp function is used to modulate the body boundary condition during some initial time steps, to ensure the smooth transition from the initial condition to the fully developed steady state. The ramp function, in fact, is a vital factor that affects the smooth development and stable evolution of properties even long after the initial period.

After the discretisation, a linear equation system, $\mathbf{Ax} = \mathbf{B}$, can be assembled, where \mathbf{A} is the left-hand matrix, \mathbf{x} is the unknown vector involving the velocity potential on the solid surfaces and the normal derivative of velocity potential on the free water surface, and \mathbf{B} is the right-hand vector that is time-varying at each time step depending on the boundary conditions. As the simulation domain is reduced to a time-invariant one in this method, the matrix \mathbf{A} is also time-invariant, as it only depends on the geometry of the computational domain. Therefore, the matrix \mathbf{A} is only assembled and solved once, which is the reason for the higher efficiency of this second-order time-domain method compared to the fully nonlinear method. To further enhance the computational efficiency, parallel computing using the OpenMP technique is also implemented in the developed numerical model.

In addition to computational efficiency, another reason for using this second-order time-domain method rather than the fully nonlinear method is the computational robustness. In the fully nonlinear method, due to the complexity of the structure geometry and the body responses, the mesh regeneration at each time step could be a very challenging task, as sometimes the intersection line between the structure surface and the free water surface is difficult to determine. However, this challenging task is avoided in the second-order time-domain method, because of the time-invariant computational domain. Furthermore, a common issue faced in the time-domain potential flow modelling is the saw-tooth numerical instability. The general idea to suppress this instability is the introduction of numerical viscosity/damping in the numerical scheme to control the amplification of numerical errors. The numerical viscosity/damping could be introduced

in many different ways, and two of the most popular approaches are the mesh regriding (Bai and Eatock Taylor 2006, Bai and Eatock Taylor 2007) and smoothing (Shao et al., 2022). Again, it is challenging to implement mesh regriding or smoothing in the fully nonlinear method, especially when the free surface geometry becomes complex. In the fully nonlinear numerical simulations, it was believed that the instability occurs because of the computational nodes moving every time step on the free surface inappropriately concentrated in certain areas, which destroys the stability condition. In this study, the computational nodes are distributed according to the requirements in terms of the resolution and mesh quality at the initial time step and become invariant in the following time steps. Therefore, the numerical instability issue is not encountered in the present study.

3. Convergence and validation

3.1. Convergence test

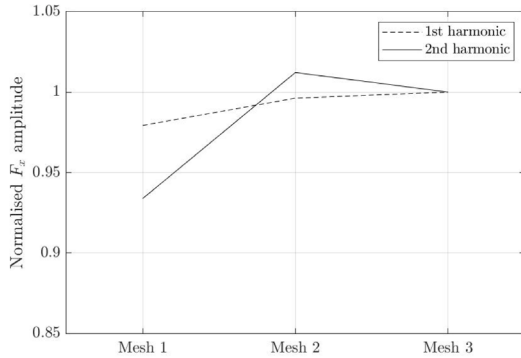
Before applying the present numerical model in the study of the suppression of near-trapping, its convergence and accuracy need to be verified. To conduct the convergence test in terms of the computational mesh and time step, a simple case of a surface-piercing vertical circular cylinder standing on the seabed in second-order Stokes waves is considered (Bai and Teng, 2013). In this case, both the water depth d and the radius of the cylinder r take the value of unity, satisfying $d/r = 1$. In addition, the incident wave amplitude A satisfies $A/L = 0.05$, where L is the wavelength, and the wave number k satisfies $kr = 1$. The modulation time T_m in the ramp function is chosen to be two incident wave periods. In addition, a circular domain is adopted in this study, where the radius of the domain including the damping zone is about $2L$. The damping zone at the outer part of the domain is of one wavelength in length for wave energy absorption.

Numerical convergence tests are carried out using three different mesh schemes. To improve computational efficiency, the non-uniform meshes are distributed on both the free water surface and the solid surfaces. On the side wall of the circular tank, the finer meshes are used near the free surface, which become coarse gradually with the water depth. The same type of mesh is also applied on the surface of the vertical circular cylinder. In addition, finer meshes can also be adopted near the bottom corner when a truncated body is considered. As the Delaunay triangulation method is used, the number of meshes cannot be specified on the free surface in this study. Instead, the number of points that are inserted in the domain is the parameter to control the number of meshes. Details of the three mesh schemes are summaries in Table 1. Note that half of the domain is considered for this case, due to the symmetry of the problem.

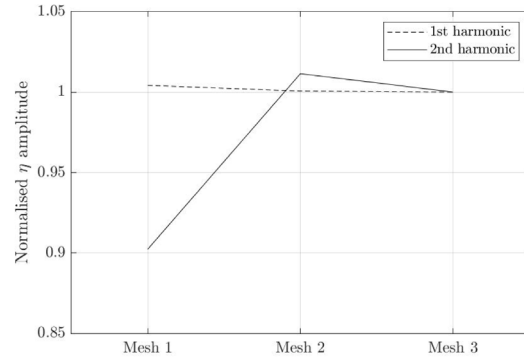
In the mesh convergence tests for different mesh schemes, the time step remains the same as $\Delta t = T/40$, where T is the incident wave period. The computations are carried out on a MacBook Pro (2020) with a 2 GHz Quad-Core Intel processor and a 16 GB Memory. According to Table 1, the computer time roughly increases quadratically with the total number of nodes in the computational domain, and all the computations are acceptable to run on a laptop with basic configurations. The mesh convergence is evaluated in terms of the wave force in the x direction on the cylinder and the wave run-up on the leeside of the cylinder. Fig. 1 shows the numerical results for these three different mesh schemes. To better show the difference, the numerical results are normalised by those for the finest mesh scheme “Mesh 3”. It is evident that the intermediate mesh scheme “Mesh 2” can provide convergent numerical results and a similar mesh density will be adopted in the following study unless stated otherwise. From the figure, it can be seen that the first-order properties can converge much faster than the second-order properties. In addition, the coarse mesh scheme “Mesh 1” can provide an acceptable approximation for the first-order properties including both the wave force and wave elevation.

Table 1
Details of three different mesh schemes for the mesh convergence test.

| Parameters | Mesh 1 | Mesh 2 | Mesh 3 |
|--|--------|--------|--------|
| Number of elements on side wall (Horizontal × Vertical) | 9 × 4 | 18 × 6 | 36 × 8 |
| Number of elements on body surface (Horizontal × Vertical) | 6 × 4 | 12 × 6 | 24 × 8 |
| Number of points inserted on free surface | 150 | 300 | 600 |
| Total number of nodes | 892 | 1963 | 4285 |
| Computer time per wave period (seconds) | 12.2 | 58.2 | 268.2 |

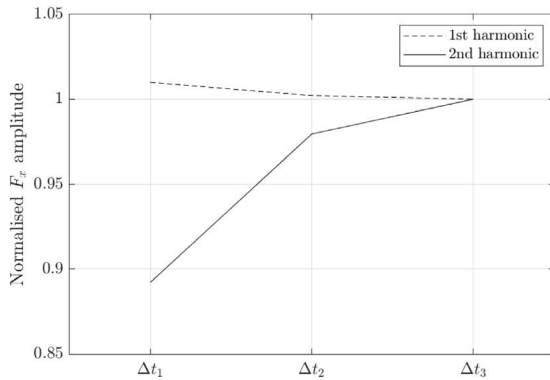


(a) Wave forces

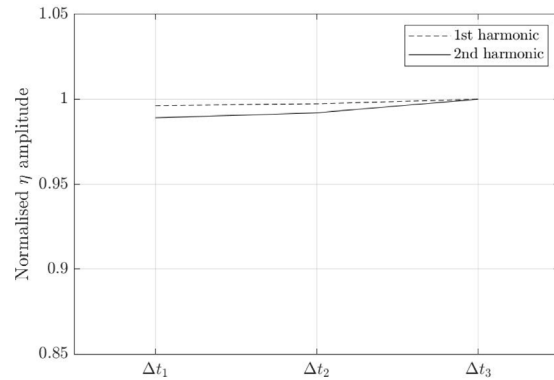


(b) Wave run-ups

Fig. 1. First and second harmonics of the normalised wave force and wave run-up for three different mesh schemes.



(a) Wave forces



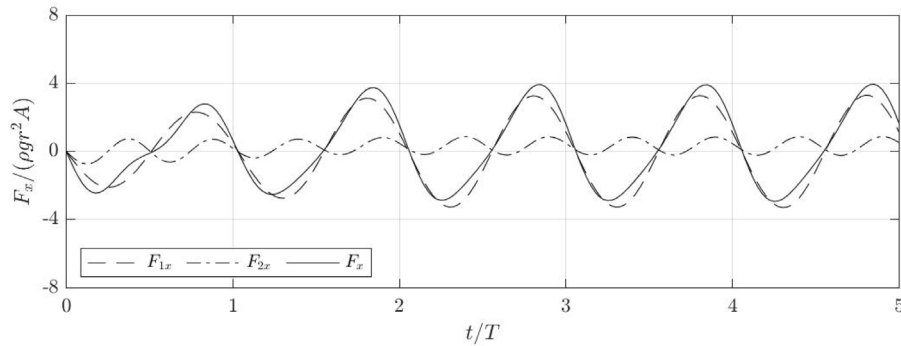
(b) Wave run-ups

Fig. 2. First and second harmonics of the normalised wave force and wave run-up at three different time steps.

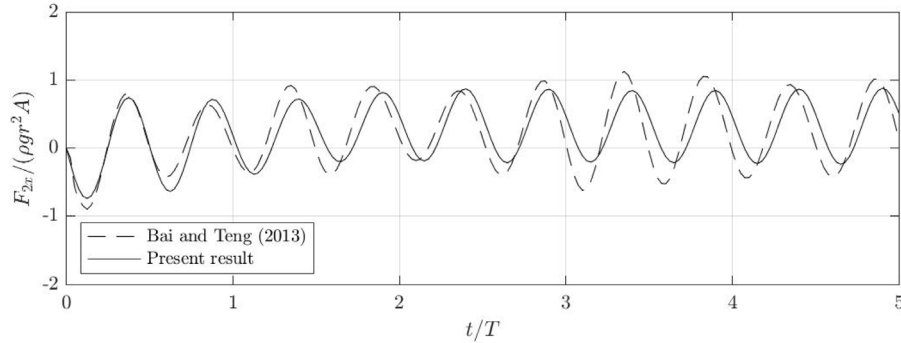
The convergence test is also conducted for different time steps with the same intermediate mesh “Mesh 2”, where the three time steps are $\Delta t_1 = T/20$, $\Delta t_2 = T/40$ and $\Delta t_3 = T/80$, and the corresponding numerical results are shown in Fig. 2. Some similar conclusions can be obtained as in the mesh convergence test, and the intermediate time step $\Delta t_2 = T/40$ will be used in the following study. However, it should be noted that the largest time step $\Delta t_1 = T/20$ seems too large for the accurate simulation of the second-order properties, given that the second-order properties oscillate at double the wave frequency, which possibly causes issues when the problem becomes more complicated.

The convergent numerical results of the horizontal wave forces with Mesh 2 and $\Delta t_2 = T/40$ are shown in Fig. 3(a), where ρ in the figure is the water density. Both the first-order and second-order wave force components reach the steady state after the modulation time of two wave periods used in the ramp function. Since the first-order result is almost identical to that in Bai and Teng (2013), only the second-order horizontal wave force component is compared to the result in Bai

and Teng (2013), as shown in Fig. 3(b). Some discrepancies can be observed, which may be caused by the different numerical methods on different mesh systems used in the simulations. However, the present numerical results look more steady, and hence more reliable. More validations are conducted in the following two sections. Furthermore, the three-dimensional wave profile in the domain is shown in Fig. 4 for the first-order and second-order components and the total second-order results. It can be seen from the figure that the second-order component is significant for this case, and the wave damping zone can work well to absorb the disturbed wave and avoid wave reflection. In the present study, the first harmonic, first-order component and first-order property represent the same results oscillating at the wave frequency obtained by solving the first-order boundary value problem. The second-order component is obtained by solving the second-order boundary value problem, while the second-order property represents the sum of the first-order property and the second-order component. The second harmonic is the property oscillating at double the wave

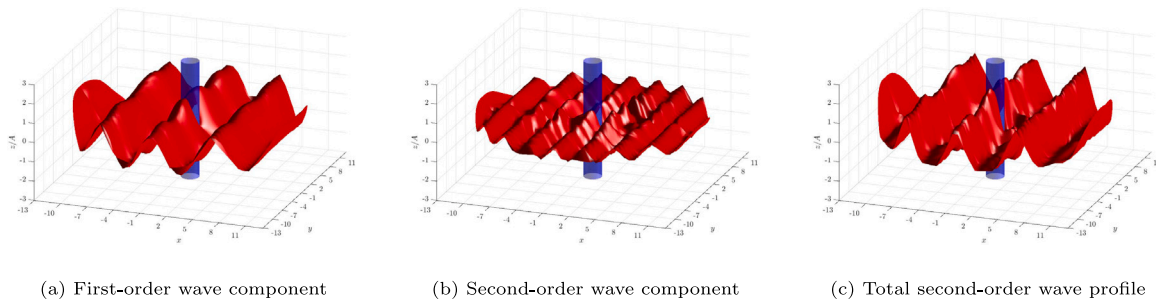


(a) First-order and second-order wave forces



(b) Comparison of second-order wave force component

Fig. 3. Time history of the horizontal wave forces on the cylinder and its comparison with published results in Bai and Teng (2013).



(a) First-order wave component

(b) Second-order wave component

(c) Total second-order wave profile

Fig. 4. First-order and second-order wave profiles at $t = 5T$.

frequency, which is obtained by taking away the mean value from the second-order component or using the FFT.

3.2. Validation of near-trapping

As the second validation test case, four vertical circular cylinders of different arrangements are considered in the regular second-order Stokes water waves. Wave profiles in the region surrounded by four cylinders standing on the seabed are the main interest in this case, and the numerical results are compared with the physical experiment in Ohl et al. (2001a), the second-order analytical solution in Malenica et al. (1999) and the fully nonlinear results in Bai et al. (2014). Two layouts of the cylinder arrangement are considered in this study, as shown in Fig. 5, where the four cylinders are located at four corners of a square of length l . In addition, two sets of physical experiments in Ohl et al. (2001a) are simulated in this study, and the numerical results are compared to the experimental data to validate the present numerical model.

The first physical experiment was conducted for a cylinder of radius $r = 0.203$ m with the distance between two cylinders of $l = 4r$. The

water depth is $d = 2.0$ m and the incident wave amplitude is $A = 0.049$ m for this case. The frequency of the incident wave is $f = 0.8$ Hz so that $kr = 0.524$ and $kA = 0.126$ for both the 0-degree and 45-degree headings. Fig. 6 shows the wave profile along the x -axis for the 0-degree wave heading and its comparison with the fully nonlinear numerical results and the experimental data. Both the maximum and mean wave elevations show two peaks: one is at the centre of the area surrounded by the cylinders, and the other is in front of the four cylinders before the wave enters the enclosed area. For the maximum wave elevation, the first-order results are significantly underestimated, whereas the second-order results demonstrate remarkable improvement due to the correction of the second-order components. The present second-order result seems smaller than the two published results, but it reproduces the small peak around $x = -0.5$ m, as shown in the experimental measurement. In addition, the trough and the right-side peak of the mean wave elevation in Fig. 6(b) are in better agreement with the experimental data than the fully nonlinear results. The same results are also shown in Fig. 7 for the 45-degree wave heading with the comparison to the published results. The wave elevation is now

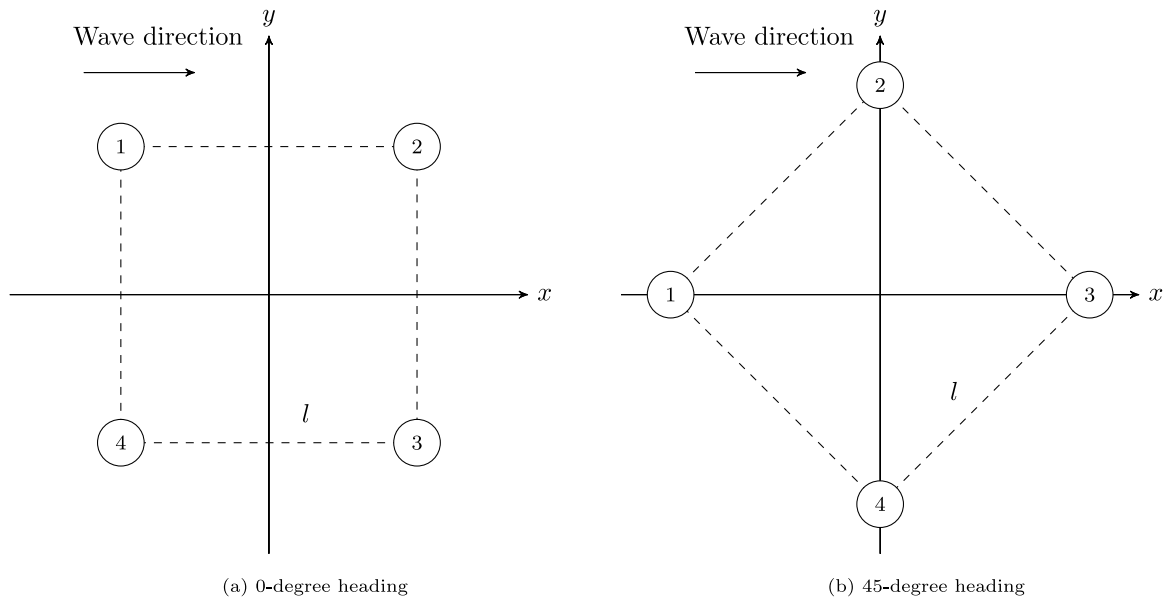


Fig. 5. Different layouts of four circular cylinders in water waves.

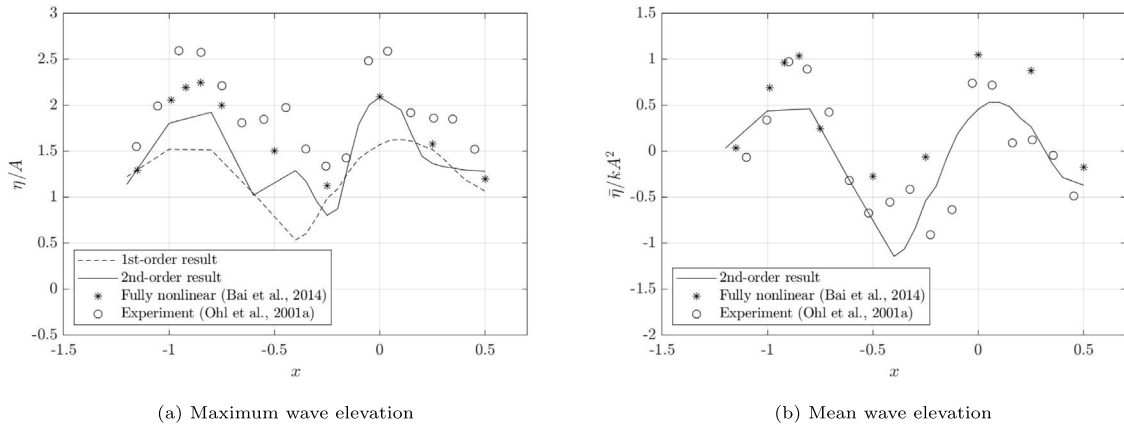


Fig. 6. Wave profile along the x -axis in the wave of 0-degree heading.

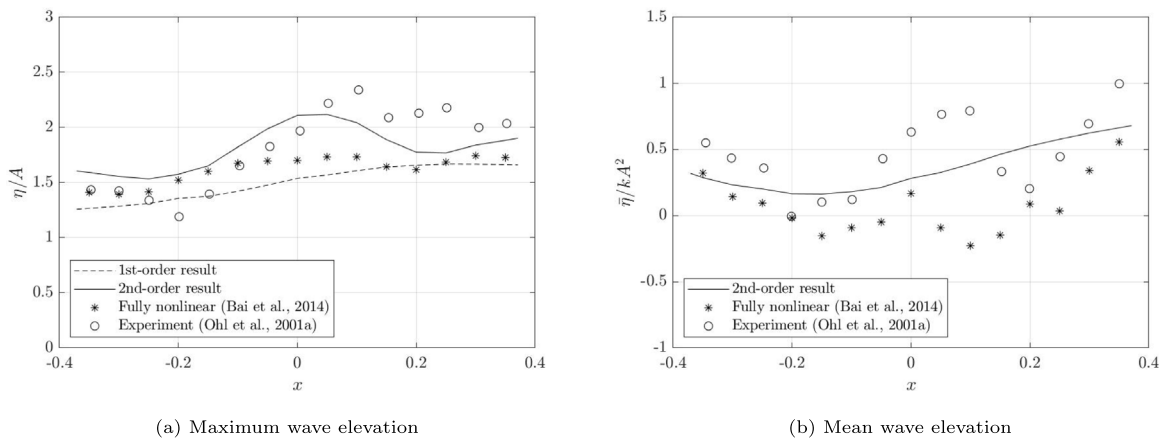


Fig. 7. Wave profile along the x -axis in the wave of 45-degree heading.

distributed along the diagonal line between Cylinders 1 and 3 shown in Fig. 5(b) which is the region enclosed by the cylinders with the inner boundaries at $x = \pm 0.371$. It can be seen from the figure that there is

no distinct peak for this case, and the present results generally agree better with the experimental data than the fully nonlinear results.

The second physical experiment considered in this study was for a cylinder of radius $r = 0.2$ m with the water depth $d = 3r$ and the same

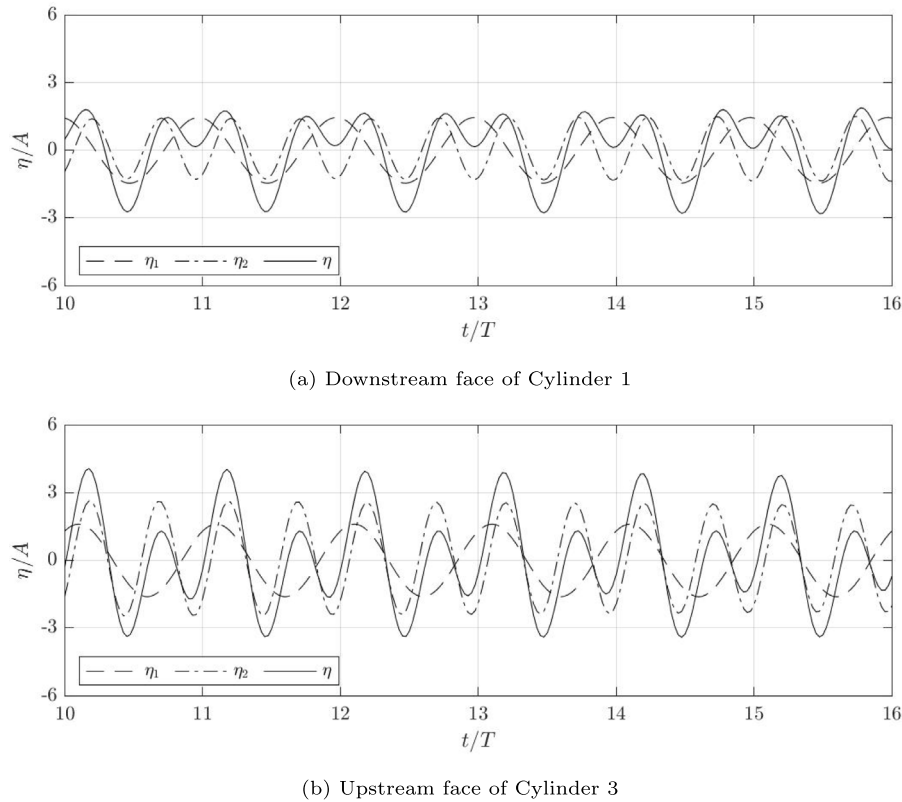


Fig. 8. Time history of the first-order and second-order wave elevations at two locations for 45-degree heading at $kr = 0.468$.

spacing ratio $l = 4r$ for the 45-degree heading situation in Fig. 5(b). In this case, the near-trapping phenomenon happens, where large wave elevations are induced at certain wave frequencies in the region enclosed by the four cylinders. This layout and configurations are the main focus of this study. Three different incident wave conditions are simulated, with the wave numbers of $kr = 1.66$, 0.754 and 0.468 that correspond to the near-trapping frequency, two-thirds and half of the near-trapping frequency for this arrangement respectively. The incident wave amplitude satisfies $kA = 0.157$ for all three wave conditions. The near-trapping frequency $kr = 1.66$ was predicted by the linear theory in Evans and Porter (1997), therefore, the first harmonic obtained by solving the first-order boundary value problem at $kr = 1.66$ can excite the near-trapping phenomenon, which is defined as the first near-trapping mode here. It is expected that the second harmonic obtained by solving the second-order boundary value problem at $kr = 0.468$ can also excite the near-trapping phenomenon, given that the second harmonic oscillates at double the wave frequency. The resonance that occurs at $kr = 0.468$ is defined as the second near-trapping mode in the present study.

In the following study, the emphasis is placed on the investigation of the second harmonic induced second near-trapping mode and its suppression. The reasons for focusing on the second near-trapping mode are twofold. In the first near-trapping mode, the wavelength at $kr = 1.66$ is even shorter than the typical size of the structure (here the distance between two cylinders l), but the wind waves encountered in the realistic offshore practice are always longer compared to the size of the structure. The other reason is that the linear solution becomes a part of the standard procedure in offshore design, which can capture the first near-trapping mode reasonably well. However, the second-order analysis could be easily omitted in offshore design, causing potential hazards to offshore structures. Good insight into the second near-trapping mode and its suppression are demanded and therefore highlighted in this study. Fig. 8 demonstrates the time history of the wave elevations right behind Cylinder 1 and in front of Cylinder 3,

where the second-order components of wave elevations are significant at both two locations. Behind the upstream Cylinder 1, the second-order component is comparable to the first-order component, whereas the second-order component becomes even larger than the first-order component in front of the downstream Cylinder 3. This is caused by the induced second near-trapping mode, which can only be captured by the second-order analysis. In this situation, it is noticed that the maximum second-order wave elevation is more than double the first-order result.

To further validate the present numerical model, the numerical results of the first harmonic, second harmonic and the mean wave profile between the upstream cylinder 1 and the downstream cylinder 3 with the inner boundaries at $x = \pm 0.366$ at the second near-trapping mode ($kr = 0.468$) are shown in Fig. 9. The comparison is made to the second-order analytical solution by Malenica et al. (1999) and the physical experimental data in Ohl et al. (2001a). It can be seen that the first harmonic and the mean wave elevation coincide well with the analytical solution. The second harmonic is generally in good agreement with the analytical solution. The difference compared to the experimental data for the second harmonic and the mean value can be observed, and its possible reason lies in the disturbance caused by the wave probes in the experiment, as discussed in Ohl et al. (2001a). The difference in the nonlinear characteristics between the present model and the experiment may also account for the discrepancy. The higher-order bound waves generated by the wave maker in the experiment are generally different from those in a Stokes wave as used in the present study.

To demonstrate clearly the first and second near-trapping modes, Fig. 10 shows the maximum wave elevations along the diagonal line between Cylinder 1 and Cylinder 3 at three different kr values. It is clear that the first harmonic of the maximum wave elevation has exceptionally large values at $kr = 1.66$, which can reach four times the incident wave amplitude, indicating the occurrence of the first near-trapping mode in Fig. 10(a). In addition, the relatively large wave elevations are excited right behind the upstream Cylinder 1 and before

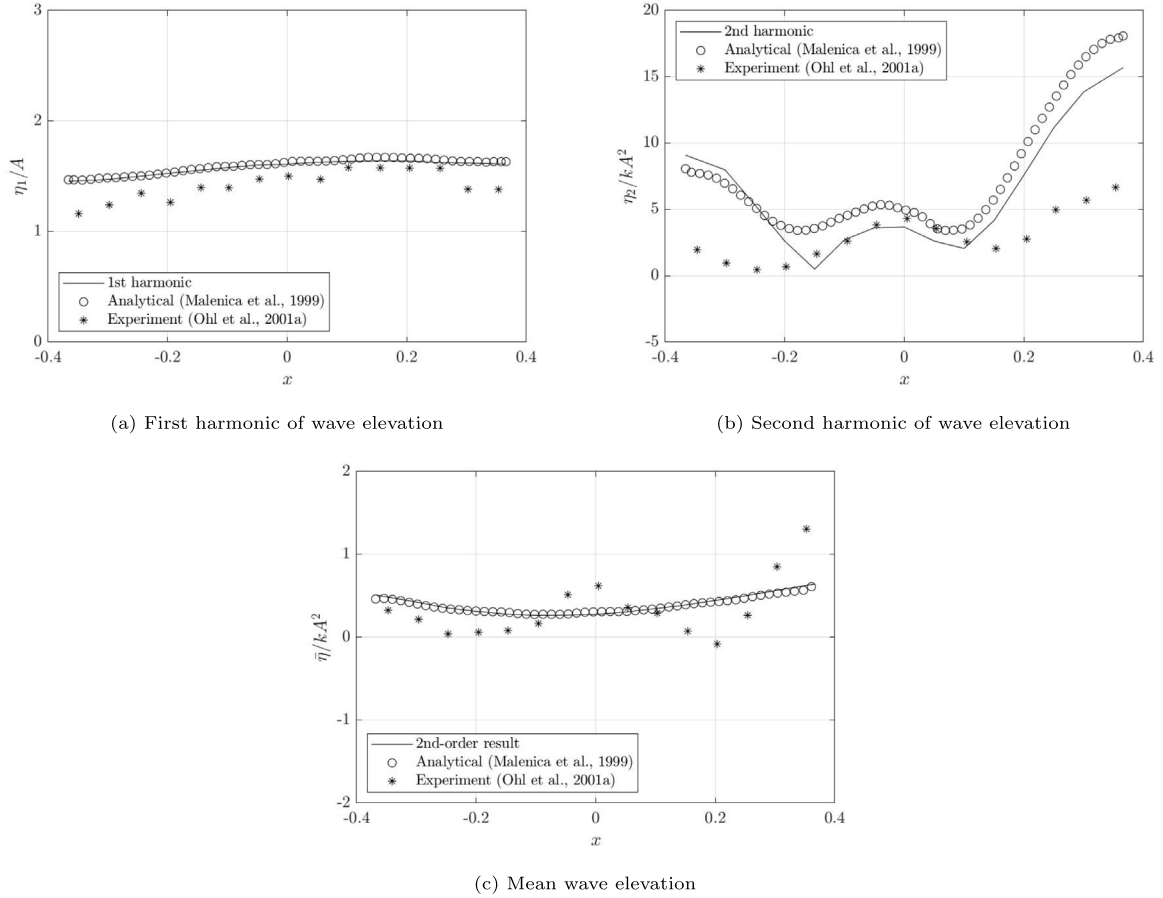


Fig. 9. Wave profile along the x -axis in the wave of 45-degree heading at $kr = 0.468$.

the downstream Cylinder 3 at the resonance frequency, whereas at the other two frequencies, the first harmonic of the maximum wave elevation is flat with a much smaller value around 1.5. The situation is changed for the second harmonic of the maximum wave elevation, as shown in Fig. 10(b), where the results at $kr = 0.468$ become much larger than those at the other two frequencies and the second near-trapping mode occurs. The shape of the second harmonic at $kr = 0.468$ is also identical to that of the first harmonic at $kr = 1.66$ since those two properties oscillate at the same frequency and the same wave resonance is excited. It is interesting to see in Fig. 10(c) that the maximum wave elevations are comparable between $kr = 1.66$ and $kr = 0.468$, which means both the first and second near-trapping modes can excite the wave resonance with the similar amplitude around four times the incident wave amplitude. In addition, over 60% of the maximum second-order wave elevation is contributed from the second harmonic at $kr = 0.468$. It highlights again that the second-order analysis is vital for predicting the maximum wave elevation when the second near-trapping mode occurs. On the other hand, the wave profiles at $kr = 0.754$ are always mild for the first and second harmonics, and the total second-order wave elevations since no resonance/trapping occurs.

4. Suppression of second harmonic induced near-trapping

4.1. Single floating truncated cylinder with motions

The discussion on the violent second near-trapping mode in the last section can naturally lead to the next question of how to suppress this resonant phenomenon, and the idea here to reduce the maximum wave elevation during the resonance is the introduction of motions into the four cylinders in Fig. 5(b), which will be discussed in the following

sections. Before the implementation of this idea, the capability of the present numerical model in modelling dynamic responses of a floating body needs to be validated. If a body is allowed to move in the translational directions only, as discussed in the present study, the body responses ξ_1 and ξ_2 in Eq. (6) need to be predicted by solving the motion equation. Using the same perturbation procedure in Section 2.1, the body motion equation can also be split into two equations ($j = 1$ or 2) for the first-order and second-order responses respectively:

$$\mathbf{M}\ddot{\xi}_j + \mathbf{K}_{\xi_j}\xi_j = \mathbf{F}_j, \quad (11)$$

where \mathbf{M} is the mass matrix, \mathbf{K} is the structural stiffness matrix associated with the mooring system and \mathbf{F} is the total force on the body. It should be noted that the wave-body interaction is a coupling problem, where the body responses are also unknown when the wave field is solved. The challenge shows up in the definition of initial conditions. The second-order Stokes wave is specified in the computational domain gradually using the ramp function, and the body velocity and acceleration are defined with zero values at the initial time step. However, the body velocity and acceleration cannot be both zero under a water wave, which means the initial condition is not compatible and the computation needs a relatively long time to find the compatible body velocity and acceleration under the given wave condition. Due to this reason, the ramping time in the ramp function for the cases with body motions is chosen as five wave periods.

A simple test case in Bai and Eatock Taylor (2009) is selected to validate the solver of the body motion equation. In this case, a truncated circular cylinder is allowed to move in the x direction only under the action of water waves propagating in the x direction. The water depth d , gravitational acceleration g and fluid density ρ_{water} are all taken to be unity, and the density of the cylinder ρ_{body} is taken

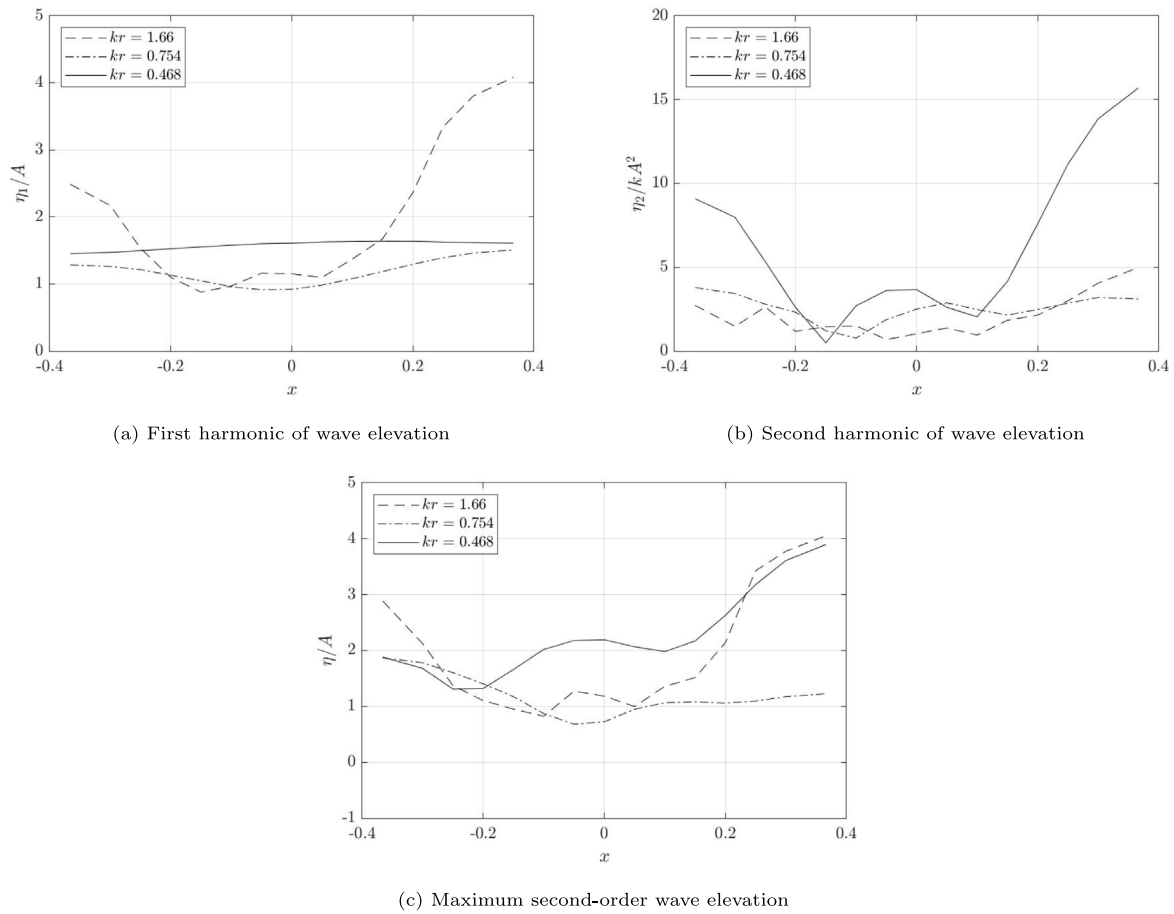


Fig. 10. Maximum wave profile along the x -axis in the wave of 45-degree heading at three different kr numbers.

the same as the water density to ensure the body can float on the water surface. The radius of the cylinder is set to be $0.15d$, and its draft is $0.6d$. To make a direct comparison with the results in Bai and Eatock Taylor (2009), the incident wave amplitude is given as $A = 0.019881d$ by using a linear transfer function to convert the motion of the wave paddle to the induced wave amplitude, and the wave number satisfies $kr = 0.6$. The wave force and body response in the x direction are shown in Fig. 11, where the first-order and second-order results and their comparison with the fully nonlinear results can be observed. Since the second-order component in the wave force is minor when the wave steepness is low in this case, the first-order and second-order wave forces are almost identical to the fully nonlinear results. However, as the body has no constraint in the x direction, any minor nonlinear component can be accumulated and cause the drift of the body in the x direction, which can be seen in Fig. 11(b). No drift can be observed in the linear solution, whereas the second-order solution is quite close to the fully nonlinear results, due to the contribution of the second-order component. The minor discrepancy is clearly due to the difference in the second-order drift, which may be caused by the different properties of the incident wave and the even higher-order components in the fully nonlinear simulation.

Since the release of motions of the cylinders in certain ways is proposed to suppress the near-trapping phenomenon, the fixed bottom-mounted system discussed in Section 3.2 needs to be adjusted to make the movement possible. To allow motion, the vertical circular cylinders need to be truncated, floating on the free surface. For the near-trapping with floating structures, the phenomenon has been demonstrated both theoretically in McIver and McIver (2006) and experimentally in Wolgamot et al. (2016). To study the effect of truncating the bottom-mounted cylinders on the near-trapping, the layout

and other configurations remain the same. The draft of the truncated cylinders is now taken as 0.4 m, given that the water depth in this case is 0.6 m. It should be noted that the system composed of four truncated cylinders is fixed for now, however, the system is still simulated using the solver developed for moving bodies. To restrain the body motion to a certain degree, one can simply set the corresponding mass in other degrees to be a very large value in the mass matrix. The approach is also used for the last test case as well as in the next section when the body is allowed to move in a specified direction only. Fig. 12 shows the comparison between the results for the bottom-mounted and truncated cylinders. For the truncated cylinders, the maximum first and second harmonics decrease in the region near the downstream cylinder 3. Due to the truncation of the downstream cylinder, more energy can radiate out of the region beneath the downstream cylinder compared to the amount of energy that enters the enclosed area, leading to a reduction in the wave elevation in this area. Nevertheless, the second harmonic of the maximum wave elevation is still significantly large in Fig. 12(a), and the second-order wave elevation is much higher than the linear solution in Fig. 12(b). All the evidence indicates that the second harmonic induced near-trapping remains remarkable even for the system with truncated cylinders, and its suppression is further studied next.

4.2. Suppression with transversal motions

Two scenarios are proposed in the present study to suppress the near-trapping, as shown in Fig. 13. In Fig. 13(a), the cylinders are allowed to move only in the directions perpendicular to the corresponding symmetric axes, which is called the motions in the transversal direction. In the second scenario in Fig. 13(b), the cylinders are allowed

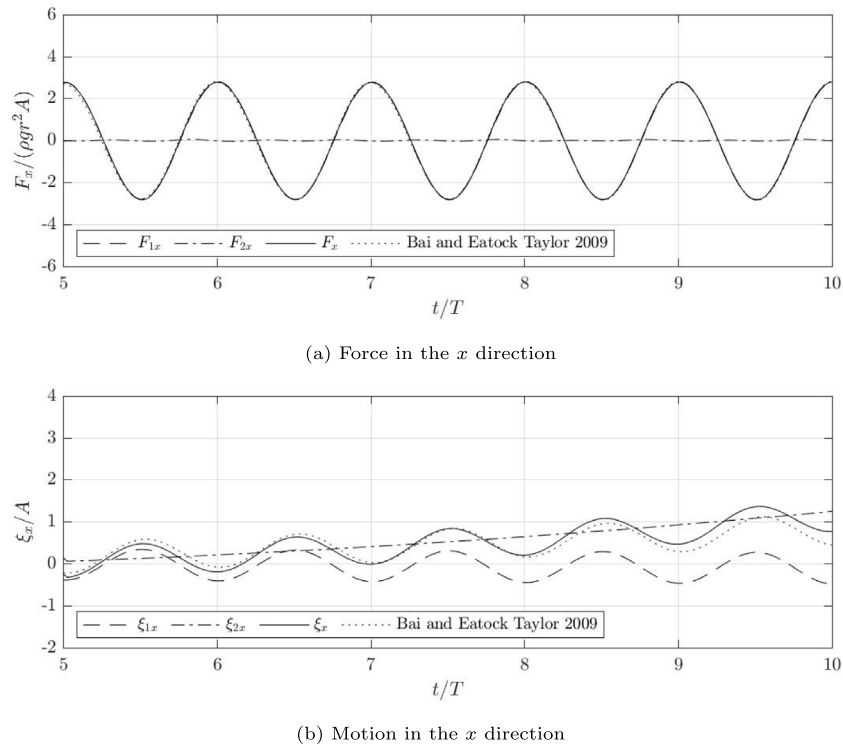


Fig. 11. Time history of the wave force and response in the x direction and their comparison with the results in Bai and Eatock Taylor (2009) at $kr = 0.6$.

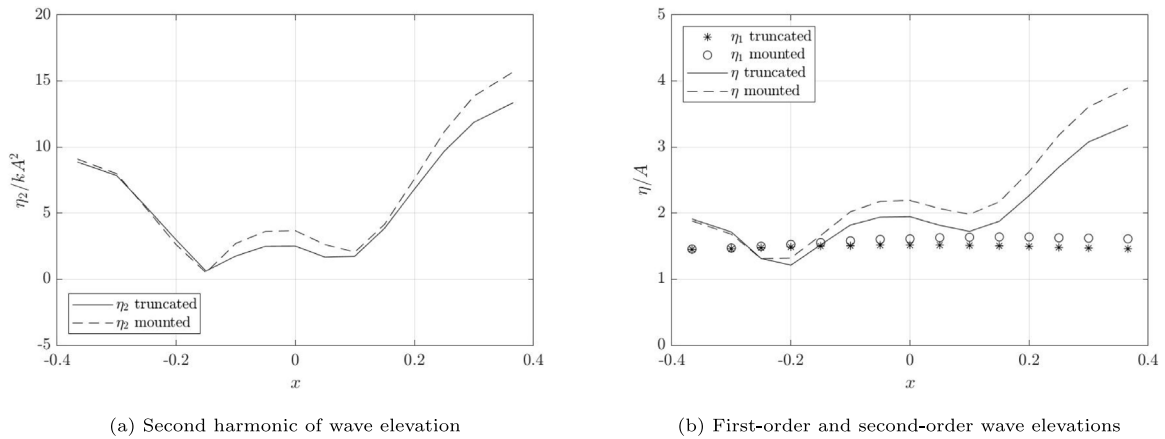


Fig. 12. Maximum wave profile along the x -axis in the wave of 45-degree heading at $kr = 0.468$ for fixed truncated cylinder.

to move only in the directions along the corresponding symmetric axes, which is defined as the motions in the longitudinal direction. It can be seen that those two scenarios do not destroy the symmetric layout of the system, which does not bring any additional difficulties during the construction and installation process and is more feasible for implementation in realistic offshore practice. A simple design, such as a smooth suspended rail can allow the minor horizontal motions of the vertical truncated cylinders without losing their functions in supporting the deck vertically. In addition, the incident wave along both the x axis and the y axis can cause near-trapping, and these two scenarios can work effectively for both two incident wave angles, as they are symmetric and insensitive to wave angles.

The fixed system with four truncated circular cylinders in the wave of 45-degree heading at $kr = 0.468$ discussed in the last section is now allowed to have the transversal motions. Due to the symmetry of the system and the incident wave angle, the upstream cylinder 1

and the downstream cylinder 3 remain stationary, and Cylinders 2 and 4 have the same motion response in the x direction. In the motion equation, the mass of the cylinders and the stiffness of the system need to be defined. To ensure the truncated cylinder can float on the water surface and produce sufficient buoyancy force to support all the equipment on the deck, the density of the cylinder is first chosen as half of the water density ($\rho_{body} = 0.5\rho_{water}$). Since there is no constraint for the body motion in the x direction in water waves, a suitable spring system needs to be introduced to ensure the motion of the cylinders is limited to a proper range. The spring constant is reflected in the stiffness matrix in the motion equation, which is defined here based on the relationship in the mass-spring system in the air where the natural frequency is defined by $\omega = \sqrt{\frac{K}{m}}$. Here K and m are the stiffness and the mass of the system, which satisfy $K = \omega^2 m$. The stiffness needs to be selected wisely, as a large stiffness can cause the system to behave like a stationary system, leading to a minor influence on the near-trapping

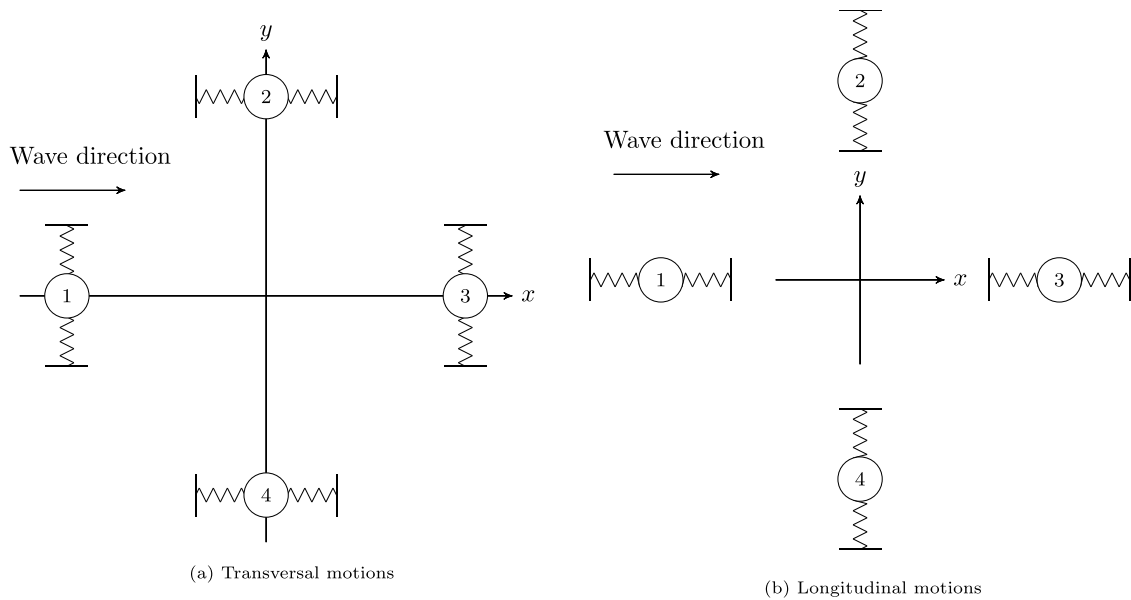


Fig. 13. Two scenarios of suppression of near-trapping.

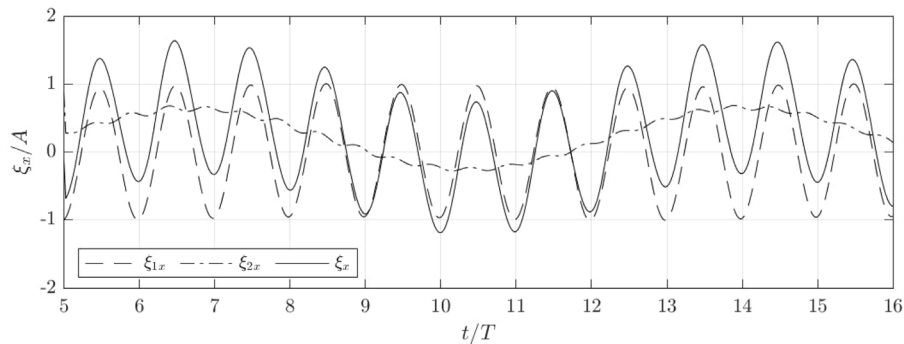


Fig. 14. Time history of the motion response of Cylinder 2 in the x direction at $kr = 0.468$ for truncated cylinders with transversal motions.

phenomenon. On the other hand, a soft stiffness cannot restrain the body motion sufficiently, which may result in the situation that the unrealistic body motion makes the design unsafe and unimplementable. The investigation starts with a K value of $0.1m$, where m is the value of the cylinder mass. The choice of the K and m values looks a bit arbitrary but is a good attempt to reveal the mechanism of the problem.

The time history of the motion response of Cylinder 2 in the x direction is shown in Fig. 14, where the first and second harmonics and the second-order solution are compared. It can be seen that the second harmonic also experiences a low-frequency oscillation, which will be discussed in the next section. In addition, the present mass and stiffness values can keep the body response in a reasonable range for small amplitude waves. Fig. 15 shows the corresponding maximum wave profile along the x direction for truncated cylinders with transversal motions. It is obvious that this scenario is not able to suppress the second harmonic induced near-trapping according to the comparison with the results for the system with four fixed truncated cylinders, as shown in Fig. 15(a). This is reasonable because the motions of Cylinder 2 and Cylinder 4 in the wave direction have barely any effect on the inner flow region enclosed by the four cylinders. The only possible influence on the wave field is the change of the phase difference between the first and second harmonics, which is reflected in Fig. 15(b) by the fact that the second-order results become smaller even with a larger second harmonic in the results. It is concluded that the scenario of allowing cylinders with transversal motions is not effective for the present problem.

4.3. Suppression with longitudinal motions

The same setup and configurations are used in this section for the system allowing cylinders with longitudinal motions to assess its effectiveness in suppressing the near-trapping. The motion responses of the cylinders are shown in Fig. 16, where Cylinders 1 and 3 move in the x direction while Cylinder 4 moves in the y direction. Since Cylinders 2 and 4 move anti-symmetrically, only the response of Cylinder 4 is shown. The motion of Cylinder 3 is slightly larger than that of Cylinder 1, but the motions of Cylinders 2 and 4 in the y direction are much smaller than those of Cylinders 1 and 3 because they are moving in the direction perpendicular to the wave direction. Due to the stiffness of the system, both the dynamic responses under transversal motions (Fig. 14) and longitudinal motions (Fig. 16) exhibit a drifting component at a very low frequency which is embedded in the second-order component. To separate the second harmonic oscillating at double the wave frequency from the low-frequency drift, the FFT method is applied to the results of the total second-order responses in Fig. 16, and the amplitude spectrum of each response is shown in Fig. 17. From the figure, one can clearly observe the positive mean drifting, in addition to a prominent low-frequency component. Since the low-frequency component oscillates with a very long period, the sample number of this component in the numerical simulations is relatively limited, compared to those for the first and second harmonics. Therefore, the frequency of this low-frequency component from the FFT analysis may involve errors. In addition, the second harmonic at Cylinder 3 is larger than that

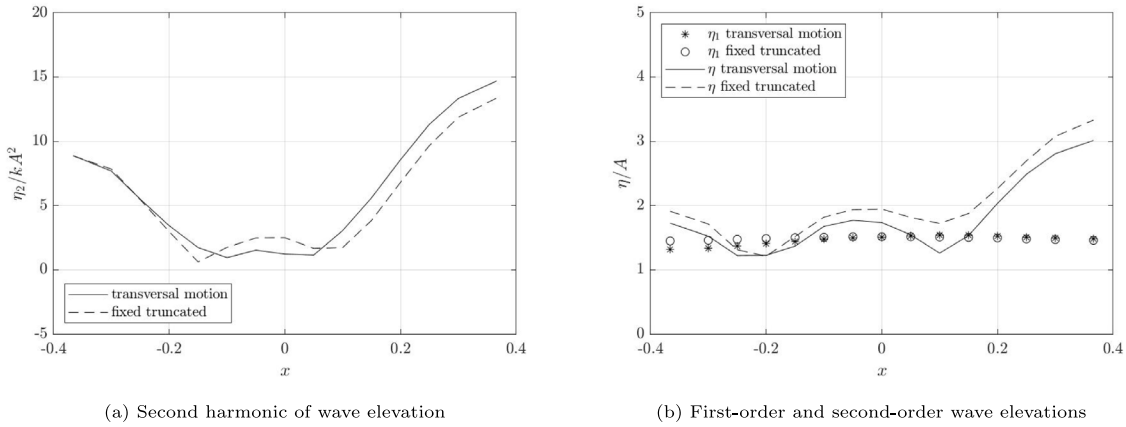


Fig. 15. Maximum wave profile along the x -axis in the wave of 45-degree heading at $kr = 0.468$ for truncated cylinders with transversal motions.

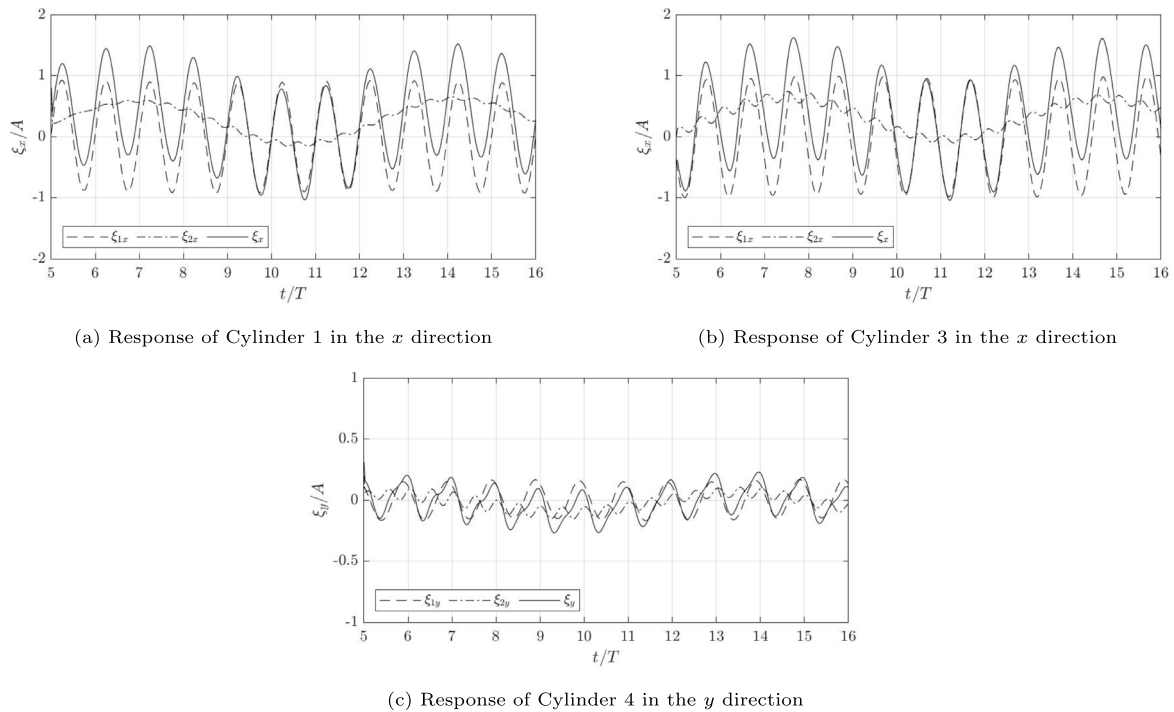


Fig. 16. Time history of the motion responses of the cylinders in the longitudinal directions at $kr = 0.468$.

at Cylinder 1, indicating the downstream cylinder experiences more nonlinearity than the upstream cylinder although the nonlinearity is small at both cylinders compared to the linear solution. The second harmonic at Cylinder 4 seems important and has a significant contribution to the total second-order solution.

Fig. 18 shows the time history of the wave elevations at the same positions as shown in Fig. 8. By comparing with Fig. 8, it can be seen that the first-order components of the wave elevations at both two locations are reduced in this scenario. In addition, the second-order component at the first position in Fig. 18(a) becomes much smaller and the total second-order wave elevation becomes first-order dominated. The second-order component at the second position in Fig. 18(b) is still comparable to the first-order component. However, because of the reduction in the first-order component, the second-order component of the wave elevation is much smaller than that in Fig. 8, which demonstrates that this scenario can effectively reduce the second harmonic induced wave near-trapping.

The effectiveness of this scenario can be further illustrated in Fig. 19, where the maximum wave profile along the x direction is compared to that for the system with four fixed truncated cylinders in Fig. 12. Fig. 19(a) shows that the second harmonic of the maximum wave elevation is reduced significantly by 86% in the region behind Cylinder 1. At the same time, in the region before Cylinder 3 the second harmonic also decreases by 63%, which indicates clearly how the cylinders with longitudinal motions can effectively suppress the second harmonic induced near-trapping. It is interesting in Fig. 19(b) that the first harmonic of the wave elevation becomes much smaller in this scenario, and in a large region before Cylinder 3 it is even smaller than the incident wave amplitude. In a large region after Cylinder 1, the second harmonic is negligible and the total second-order wave elevation is also close to the incident wave amplitude. Due to the contribution of the second harmonic before Cylinder 3, the total second-order wave elevation is relatively large, but it still reduces by 59% compared to the fixed truncated-cylinder system. The

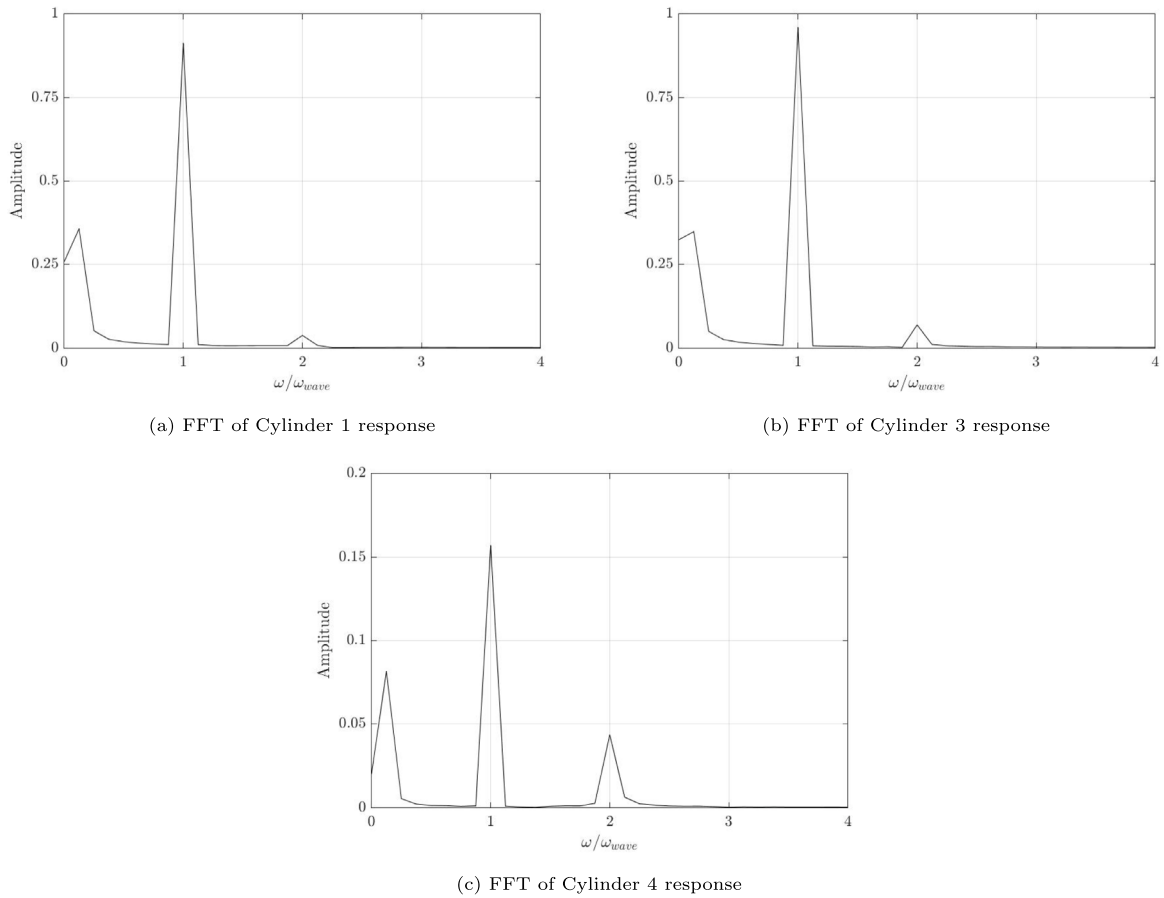


Fig. 17. FFT analysis of the motion responses of the cylinders in the longitudinal directions at $kr = 0.468$.

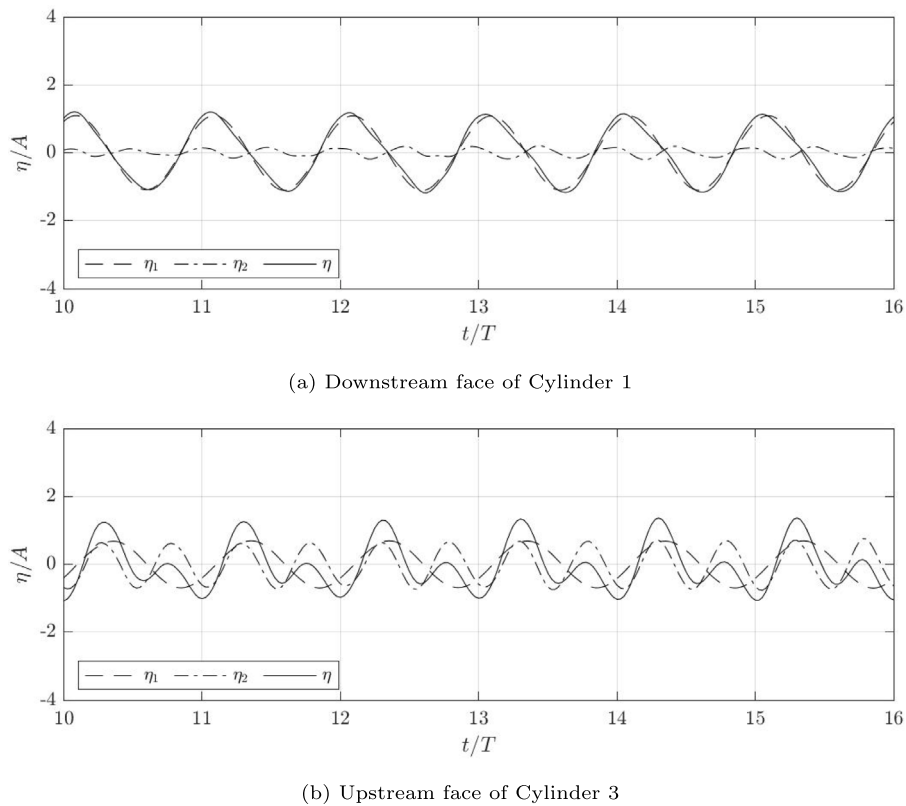


Fig. 18. Time history of the first-order and second-order wave elevations at two locations for 45-degree heading at $kr = 0.468$ for truncated cylinders with longitudinal motions.

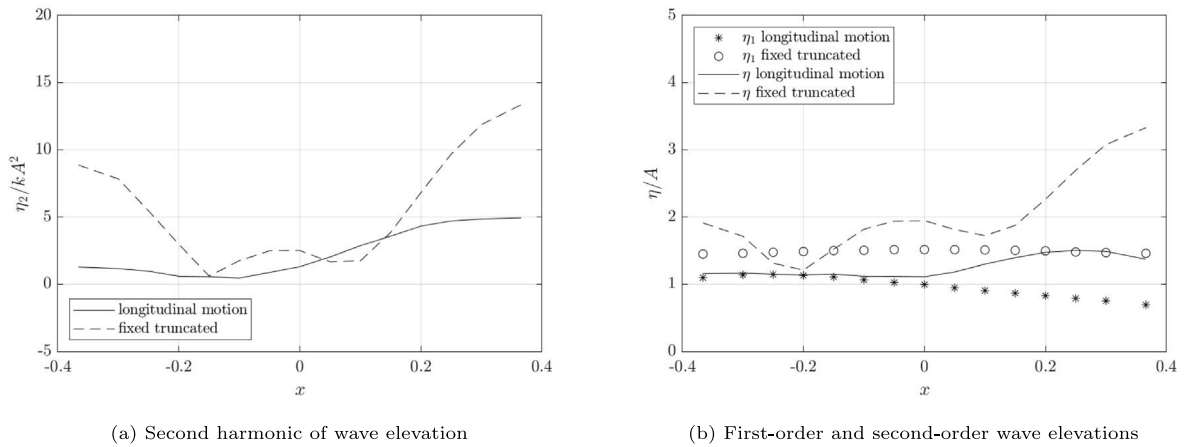


Fig. 19. Maximum wave profile along the x -axis in the wave of 45-degree heading at $kr = 0.468$ for truncated cylinders with longitudinal motions.

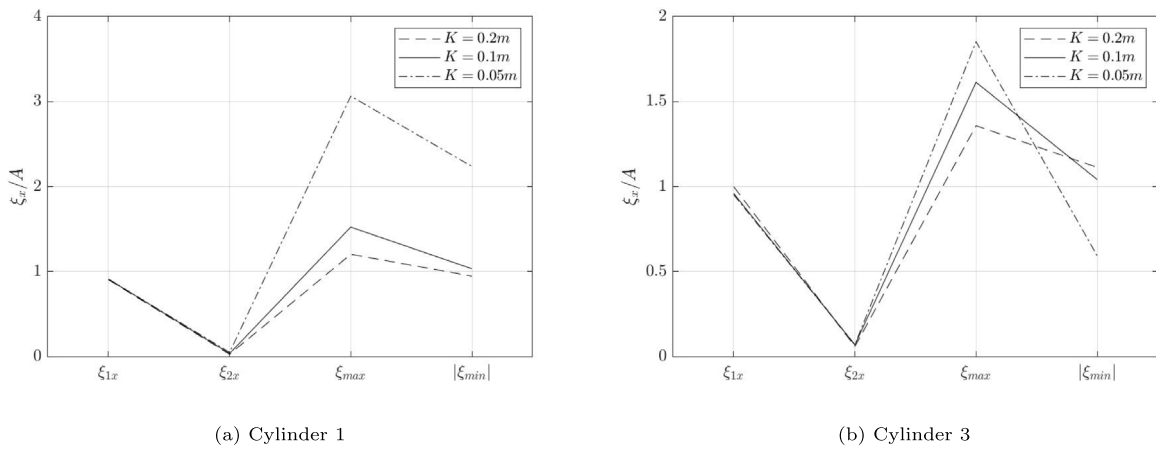


Fig. 20. Responses of two cylinders at $kr = 0.468$ for truncated cylinders with three different stiffness values.

suppression of the near-trapping in this scenario is not a surprise, because the body motion can absorb some wave energy, and less energy in the wave field can lead to the reduction in the wave elevation. The reflection wave from Cylinder 3 can also superimpose on the wave field and further reduce the wave elevation when the reflection wave has a suitable phase difference to the coming wave field. Furthermore, as the near-trapping frequency is dependent on the distance between Cylinder 1 and Cylinder 3, the change of distance between them due to their longitudinal motions may effectively destroy the near-trapping formation mechanism.

4.4. Influence of mass and stiffness

The effectiveness of allowing cylinders to have longitudinal motions in suppressing the second harmonic induced near-trapping has been demonstrated in the last section for $\rho = 0.5\rho_{water}$ and $K = 0.1m$. This work is further extended to evaluate the effectiveness of this scenario under different body mass and stiffness values. Three different stiffness values, $K = 0.2m, 0.1m$ and $0.05m$, and three different mass values, $\rho = 0.3\rho_{water}, 0.5\rho_{water}$ and $0.7\rho_{water}$ are considered in this study. Firstly, the dynamic responses of the cylinders under various stiffnesses with the same mass of $\rho = 0.5\rho_{water}$ are shown in Fig. 20, where the first and second harmonics from the FFT analysis, and the maximum and minimum displacements are presented. As Cylinders 2 and 4 experience smaller responses, thus only the results for Cylinders 1 and 3 are shown in the figure. From the figure, it is interesting to see that the first and second harmonics of the dynamic responses

are independent of the stiffness. As the incident wave is the same, the oscillating components in the first order and the second order remain the same in both the input wave and the output dynamic response. The influence of the stiffness is shown in the amplitude of the drifting motion, which is also the main influence in the maximum and minimum responses. It is obvious that smaller stiffness can lead to larger drifting and hence larger maximum displacement. In addition, the mean position of the displacement shows that the cylinders drift in the downstream direction. Cylinder 3 experiences slightly larger maximum displacements than Cylinder 1 at larger stiffness, but the maximum response of Cylinder 1 becomes much larger than Cylinder 3 at smaller stiffnesses. The maximum wave profile along the x axis is also shown in Fig. 21, where the first and second harmonics and the total second-order wave elevations are presented. The significant outcome from the results is that the wave profile is independent of the stiffness of the system. The change of the stiffness mainly affects the low-frequency drift of the cylinders, but the low-frequency motions seem not to produce any harmonic components of the wave field at the first and second harmonic frequencies.

The mass of the cylinder is also varied with the same stiffness of $K = 0.1m$, and the corresponding dynamic responses and wave profiles are shown in Figs. 22 and 23, respectively. Under various masses, the second harmonics of the dynamic responses are very close, but the first harmonics can find the difference that heavier mass causes smaller responses. In addition, as the cylinder with the smaller mass also has a smaller stiffness, Cylinder 1 in this case experiences a very large drift, whereas the drift of Cylinder 3 is much smaller. The influence

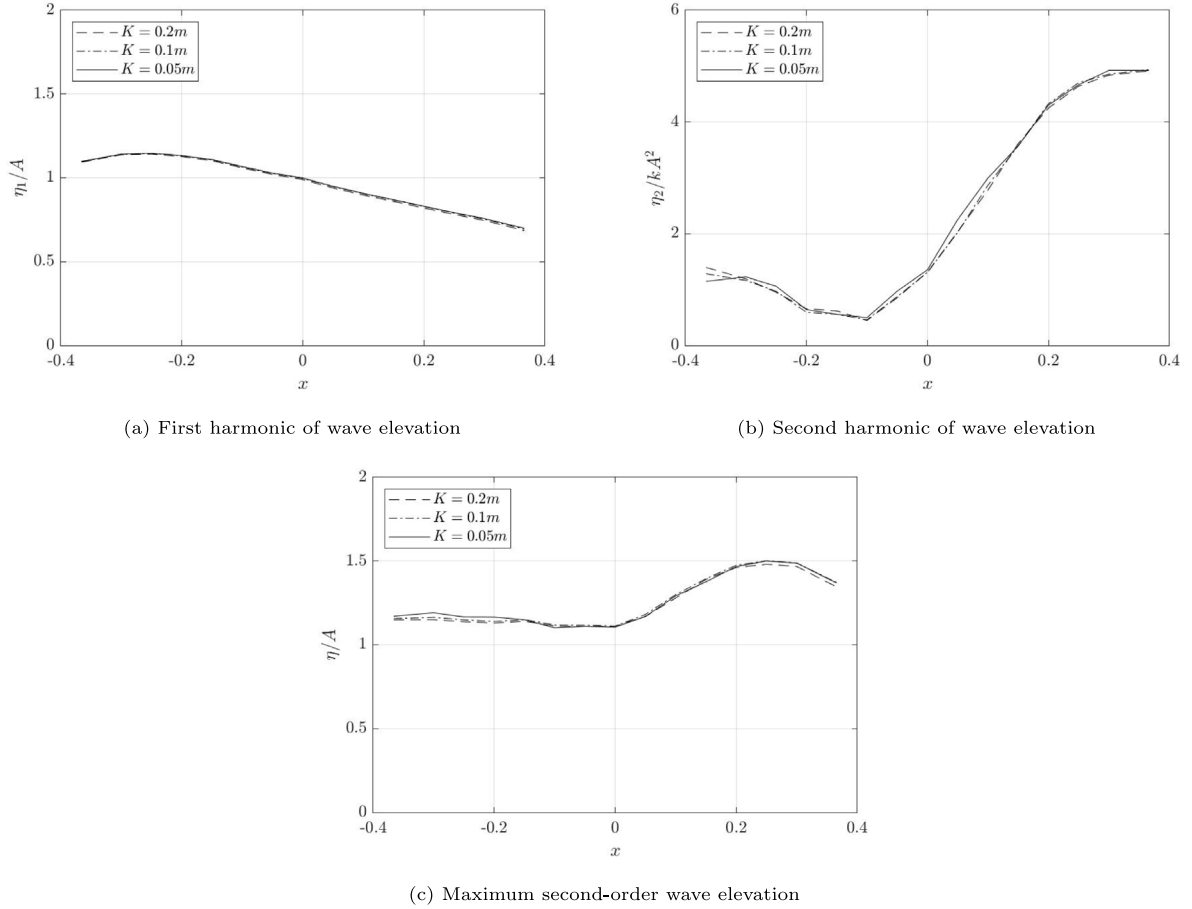


Fig. 21. Maximum wave profile along the x -axis in the wave of 45-degree heading at $kr = 0.468$ for truncated cylinders with three different stiffness values.

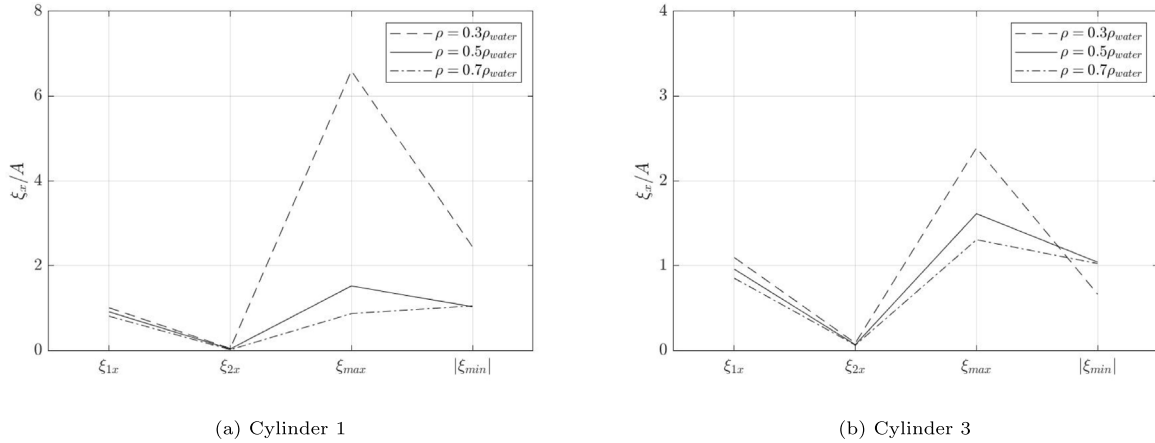


Fig. 22. Responses of two cylinders at $kr = 0.468$ for truncated cylinders with three different mass values.

of the mass can also be found in the wave profile, where the larger mass can induce the larger first harmonic and total second-order wave elevation. However, the larger second harmonic of the wave elevation is distributed around the cylinders with a smaller mass. In general, the mass influence on the wave profile seems not very significant.

4.5. Shift of near-trapping frequency

The results presented above are mainly for the second near-trapping mode at $kr = 0.468$, where significant reduction can be observed in the wave profile with the suppression scenario proposed in this study.

However, this second near-trapping frequency is determined for the four fixed cylinders, which could shift to a nearby frequency when the cylinders undergo horizontal motions. To identify if the near-trapping frequency shifts and understand how the frequency shift affects the effectiveness of the wave suppression, several kr numbers around the second near-trapping frequency at $kr = 0.468$ are tested for the same mass and stiffness as presented in Fig. 19. It can be seen in Fig. 19 that the largest wave occurs just in front of the downstream Cylinder 3, therefore, the first-order and second-order wave elevations at this location are shown against the kr number in Fig. 24. In addition,

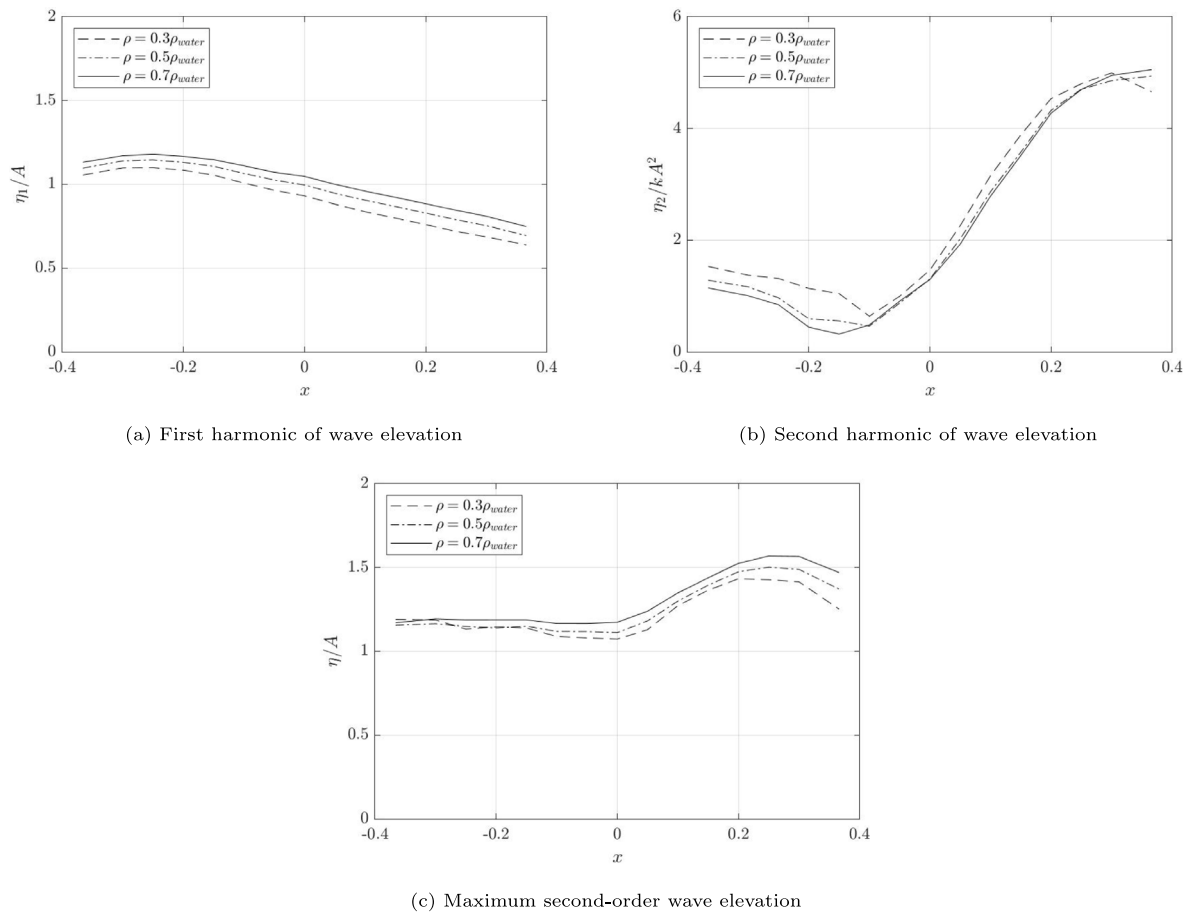


Fig. 23. Maximum wave profile along the x -axis in the wave of 45-degree heading at $kr = 0.468$ for truncated cylinders with three different mass values.

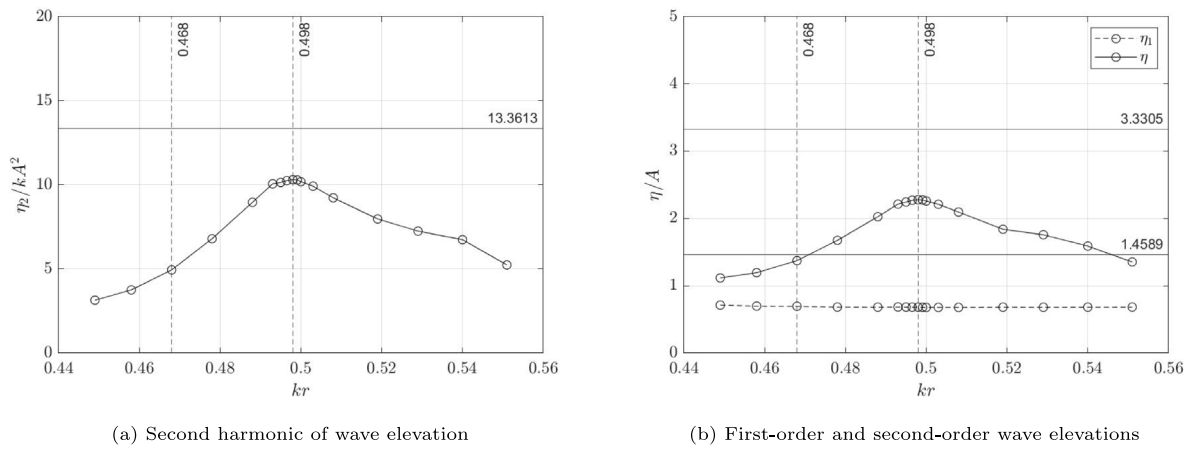


Fig. 24. Wave elevation in front of Cylinder 3 at various kr numbers for truncated cylinders with longitudinal motions.

to accurately capture the shifted near-trapping frequency, more kr numbers are selected around the peak values.

From the figure, it is clear that the second near-trapping frequency shifts from $kr = 0.468$ to $kr = 0.498$, which implies that the longitudinal oscillating motions of the cylinders, as shown in Fig. 16, can have a considerable effect on the resonant frequency. This is an interesting finding of this study. The numbers above the horizontal solid lines in the figure show the corresponding values for the case of the fixed cylinders without the suppression scenario for a direct comparison. Due to the shift of the resonant frequency, the reduction in the second harmonic becomes smaller (23%) at the shifted near-trapping frequency than that at the

near-trapping frequency for the fixed cylinders (63%) with the same suppression scenario. This is still a remarkable suppression of second harmonic induced near-trapping using the scenario proposed in this study, even with a shift in the near-trapping frequency. The first-order wave elevation seems not to be affected by the shift of the second near-trapping frequency, since those frequencies in Fig. 24 are quite far from the first near-trapping frequency. However, a significant reduction in the first-order wave elevation can be observed, which provides a major contribution to the reduction in the total second-order wave elevation. It is indicated that the scenario proposed in this study can also work well in suppressing the first-order properties. The second-order wave

elevation at the shifted near-trapping frequency is reduced by 32%, demonstrating that the proposed scenario can effectively suppress the second harmonic induced near-trapping phenomenon.

5. Conclusion

A second-order potential flow model is solved numerically in the time domain using the high-order boundary element method to study the suppression of the near-trapping waves around a cylinder array. The convergence of the developed numerical model is tested through a simple case of wave diffraction around a single vertical circular cylinder, from which it can be seen that the results converge fast with the computational mesh and time step. The numerical model is further validated by the study of near-trapping around an array of four circular cylinders in two different arrangements. The good agreement with the others' analytical solution, experimental data and numerical results indicates the accuracy of the numerical model. Especially, the second harmonic induced near-trapping can be captured well, which is the main event to be suppressed in this study.

The main idea for the suppression of near-trapping is to allow the cylinders to move in a certain way by introducing the mass-spring system. After validating the solver for the body dynamic responses using a single cylinder, the numerical model is used to test two scenarios: the cylinders undergoing transversal and longitudinal motions with respect to the symmetric axes. The scenario of transversal motions does not work in the suppression of near-trapping, whereas the scenario of longitudinal motions shows that it is very effective for this purpose. Large reductions in the wave profile can be observed for both the maximum second harmonic (63%) and the maximum total second-order results (59%) at the near-trapping frequency. It is interesting to see that the first-order wave profile also experiences the reduction, and it becomes even smaller than the incident wave amplitude in a large portion of the enclosed region. Various masses and stiffnesses of the cylinders are also examined, and the numerical results reveal that the wave profile does not change much for the parameters considered in this study as long as the cylinders are allowed to move in the longitudinal direction. In addition, the near-trapping frequency can shift to a nearby frequency when the cylinders are allowed to move, but the proposed scenario is still effective in the suppression of the second harmonic induced near-trapping.

CRedit authorship contribution statement

Wei Bai: Writing – review & editing, Writing – original draft, Methodology, Investigation, Conceptualization, Software. **Xingya Feng:** Writing – review & editing, Methodology, Investigation. **Sheng-Chao Jiang:** Writing – review & editing, Methodology, Investigation. **Peiwen Cong:** Writing – review & editing, Methodology, Investigation. **Ling Qian:** Writing – review & editing, Methodology, Investigation.

Declaration of competing interest

The authors declare that they have no known competing financial interests or personal relationships that could have appeared to influence the work reported in this paper.

Data availability

Data will be made available on request.

References

- Bai, W., Eatock Taylor, R., 2006. Higher-order boundary element simulation of fully nonlinear wave radiation by oscillating vertical cylinders. *Appl. Ocean Res.* 28, 247–265.
- Bai, W., Eatock Taylor, R., 2007. Numerical simulation of fully nonlinear regular and focused wave diffraction around a vertical cylinder using domain decomposition. *Appl. Ocean Res.* 29, 55–71.
- Bai, W., Eatock Taylor, R., 2009. Fully nonlinear simulation of wave interaction with fixed and floating flared structures. *Ocean Eng.* 36, 223–236.
- Bai, W., Feng, X., Eatock Taylor, R., Ang, K.K., 2014. Fully nonlinear analysis of near-trapping phenomenon around an array of cylinders. *Appl. Ocean Res.* 44, 71–81.
- Bai, W., Teng, B., 2013. Simulation of second-order wave interaction with fixed and floating structures in time domain. *Ocean Eng.* 74, 168–177.
- Chatjigeorgiou, I.K., Katsardi, V., 2018. Hydrodynamics and near trapping effects in arrays of multiple elliptical cylinders in waves. *Ocean Eng.* 157, 121–139.
- Chen, J.T., Wu, C.F., Chen, I.L., Lee, J.W., 2012. On near-trapped modes and fictitious frequencies for water wave problems containing an array of circular cylinders using a null-field boundary integral equation. *Eur. J. Mech. B Fluids* 32, 32–44.
- Cong, P., Zhao, M., Teng, B., Gou, Y., Liu, Y., 2023. Second-order near trapping of water waves by a square array of vertical columns in bi-chromatic seas. *J. Fluids Struct.* 121, 103916.
- Contento, G., D'Este, F., Sicchiero, M., Codiglia, R., Calzá, M., 2005. Run-up and wave forces on an array of vertical circular cylinders: experimental study on the second-order near trapping. *Int. J. Offshore Polar Eng.* 15 (2), 96–103.
- Evans, D., Porter, R., 1997. Near-trapping of waves by circular arrays of vertical cylinders. *Appl. Ocean Res.* 19 (2), 83–99.
- Grice, J.R., Taylor, P.H., Eatock Taylor, R., 2013. Near-trapping effects for multi-column structures in deterministic and random waves. *Ocean Eng.* 58, 60–77.
- Grice, J.R., Taylor, P.H., Eatock Taylor, R., Zang, J., Walker, D.A.G., 2015. Extreme wave elevations beneath offshore platforms, second order trapping, and the near flat form of the quadratic transfer functions. *Comput. & Fluids* 119, 13–25.
- Isaacson, M., Cheung, K.F., 1992. Time-domain second-order wave diffraction in three dimensions. *J. Waterway Port Coast. Ocean Eng.* 118 (5), 496–516.
- Isaacson, M., Ng, J.Y.T., 1995. Time-domain second-order wave interaction with three-dimensional floating bodies. *Int. J. Offshore Polar Eng.* 5 (3), 171–179.
- Kang, Y., Zeng, X., Cui, Z., Chen, J., 2024. Analytical solutions for hydrodynamic responses of arrays of floating truncated cylinders using multi-term Galerkin method and its application to a new wave energy converter device. *Phys. Fluids* 36 (5), 057101.
- Konispoliatis, D.N., 2023. Near trapping phenomena in arrays of porous vertical cylinders. *Phys. Fluids* 35 (9), 093607.
- Konispoliatis, D.N., Chatjigeorgiou, I.K., Mavrakos, S.A., 2020. Near trapped wave phenomena in an array of truncated cylinders in a perpendicular arrangement in front of a vertical breakwater. *Appl. Math. Model.* 83, 497–525.
- Li, A.-j., Liu, Y., Fang, H., 2023. Wave scattering by porous cylinders with inner columns near a vertical wall. *Phys. Fluids* 35 (8), 087111.
- Lin, Z., Pokrajac, D., Guo, Y., Liao, C., Tang, T., 2020. Near-trapping effect of wave-cylinders interaction on pore water pressure and liquefaction around a cylinder array. *Ocean Eng.* 218, 108047.
- Malenica, S., Eatock Taylor, R., Huang, J.B., 1999. Second-order water wave diffraction by an array of vertical cylinders. *J. Fluid Mech.* 390, 349–373.
- Maniar, H.D., Newman, J.N., 1997. Wave diffraction by a long array of cylinders. *J. Fluid Mech.* 339, 309–330.
- McIver, P., McIver, M., 2006. Trapped modes in the water-wave problem for a freely floating structure. *J. Fluid Mech.* 558, 53–67.
- Meylan, M.H., Eatock Taylor, R., 2009. Time-dependent water-wave scattering by arrays of cylinders and the approximation of near trapping. *J. Fluid Mech.* 631, 103–125.
- Ning, D., Xu, J., Chen, L., Cong, P., Zhao, M., Jiang, C., 2022. Boussinesq modelling of near-trapping in a four-cylinder array. *Ocean Eng.* 248, 110767.
- Ohl, C.O.G., Eatock Taylor, R., Taylor, P.H., Borthwick, A.G.L., 2001a. Water wave diffraction by a cylinder array. Part 1. Regular waves. *J. Fluid Mech.* 442, 1–32.
- Ohl, C.O.G., Taylor, P.H., Eatock Taylor, R., Borthwick, A.G.L., 2001b. Water wave diffraction by a cylinder array. Part 2. Irregular waves. *J. Fluid Mech.* 442, 33–66.
- Ren, X., Tao, L., Liang, Y., Han, D., 2021. Nonlinear wave surface elevation around a multi-column offshore structure. *Ocean Eng.* 238, 109757.
- Shao, Y.L., Faltinsen, O.M., 2010. Use of body-fixed coordinate system in analysis of weakly nonlinear wave-body problems. *Appl. Ocean Res.* 32, 20–33.
- Shao, Y., Zheng, Z., Liang, H., Chen, J., 2022. A consistent second-order hydrodynamic model in the time domain for floating structures with large horizontal motions. *Comput.-Aided Civ. Infrastruct. Eng.* 37, 894–914.
- Walker, D.A.G., Eatock Taylor, R., Taylor, P.H., Zang, J., 2008. Wave diffraction and near-trapping by a multi-column gravity-based structure. *Ocean Eng.* 35, 201–229.
- Wang, C.Z., Ren, J.M., Yang, Y.F., Ge, H., 2024. Nonlinear wave resonance by four bottom-mounted cylinders in a uniform current using a higher order finite element method. *Appl. Ocean Res.* 150, 104125.
- Wang, C.Z., Wu, G.X., 2007. Time domain analysis of second-order wave diffraction by an array of vertical cylinders. *J. Fluids Struct.* 23 (4), 605–631.
- Wolgamot, H.A., Taylor, P.H., Eatock Taylor, R., van den Bremer, T.S., Raby, A.C., Whittaker, C., 2016. Experimental observation of a near-motion-trapped mode: free motion in wave with negligible radiation. *J. Fluid Mech.* 786, R5.
- Yang, Y.F., Wang, C.Z., 2020. Finite element analysis of second order wave resonance by multiple cylinders in a uniform current. *Appl. Ocean Res.* 100, 102132.